AEDC-TR-79-6

Applications of the Aerotherm
BLIMP Boundary-Layer Program
to Nonablating Reentry Flight Conditions

Emmett E. Edenfield
ARO, Inc.

July 1979

Final Report for Period March — August 1978

Approved for public release; distribution unlimited.

ARNOLD ENGINEERING DEVELOPMENT CENTER
ARNOLD AIR FORCE STATION, TENNESSEE
AIR FORCE SYSTEMS COMMAND
UNITED STATES AIR FORCE

This report has been reviewed by the Information Office (OI) and is releasable to the National Technical Information Service (NTIS). At NTIS, it will be available to the general public, including foreign nations.

APPROVAL STATEMENT

This report has been reviewed and approved.

ELTON R. THOMPSON
Project Manager, Research Division
Directorate of Test Engineering

Approved for publication:

FOR THE COMMANDER

ROBERT W. CROSSLEY, Lt Colonel, USAF
Acting Director of Test Engineering
Deputy for Operations

REPORT DOCUMENTATION PAGE		READ INSTRUCTIONS BEFORE COMPLETING FORM
1 REPORT NUMBER AEDC-TR-79-6	2 GOVT ACCESSION NO.	3 RECIPIENT'S CATALOG NUMBER
4 TITLE (and Subtitle) APPLICATIONS OF THE AEROTHERM BLIMP BOUNDARY-LAYER PROGRAM TO NONABLATING REENTRY FLIGHT CONDITIONS		5 TYPE OF REPORT & PERIOD COVERED Final Report, March – August 1978
		6 PERFORMING ORG. REPORT NUMBER
7 AUTHOR(s) Emmett E. Edenfield, ARO, Inc., a Sverdrup Corporation Company		8 CONTRACT OR GRANT NUMBER(s)
9 PERFORMING ORGANIZATION NAME AND ADDRESS Arnold Engineering Development Center/DOT Air Force Systems Command Arnold Air Force Station, Tennessee 37389		10. PROGRAM ELEMENT, PROJECT, TASK AREA & WORK UNIT NUMBERS Program Element 65807F
11 CONTROLLING OFFICE NAME AND ADDRESS Arnold Engineering Development Center/OIS Air Force Systems Command Arnold Air Force Station, Tennessee 37389		12 REPORT DATE July 1979
		13 NUMBER OF PAGES 68
14 MONITORING AGENCY NAME & ADDRESS(If different from Controlling Office)		15 SECURITY CLASS. (of this report) UNCLASSIFIED
		15a DECLASSIFICATION/DOWNGRADING SCHEDULE N/A

16 DISTRIBUTION STATEMENT (of this Report)

Approved for public release; distribution unlimited.

17 DISTRIBUTION STATEMENT (of the abstract entered in Block 20, if different from Report)

18 SUPPLEMENTARY NOTES

Available in DDC

19. KEY WORDS (Continue on reverse side if necessary and identify by block number)

conical bodies	analysis
boundary layer	laminar flow
reentry vehicles	turbulent flow
heat transfer	hypersonic flow
theory	

20 ABSTRACT (Continue on reverse side if necessary and identify by block number)
The Aerotherm Boundary Layer Integral Matrix Procedure (BLIMP) code was applied to several nonablating reentry flight situations, and the results were compared with flight data (the Reentry F flight) and theoretical results from other sophisticated flow-field calculation techniques. Theoretical comparisons were made with results from the Lubard-Helliwell fully viscous shock layer code, the Patankar-Spalding boundary-layer code, and for sharp cones, the

DD FORM 1473 1 JAN 73 EDITION OF 1 NOV 65 IS OBSOLETE

20. ABSTRACT (Continued)

Adams three-dimensional windward plane of symmetry code. Results
indicate that the turbulence model currently in the BLIMP code
tends to overpredict heat-transfer rates at reentry (nonablating)
conditions, and that the Cebeci-Smith turbulence model should be
used in BLIMP instead.   This is consistent with results previ-
ously reported by R. Michael Evans of Aerotherm for rocket nozzle
flows.   Good comparisons of turbulent heat-transfer rates with
flight results were obtained using the Cebeci-Smith turbulence
model in BLIMP, and reasonable comparisons with the other theories
are also shown.   Under laminar, perfect gas flow conditions (where
the thermodynamic and transport properties were identical), BLIMP
calculations compared very well with the other theoretical methods
for both sharp and slightly blunted cones, at Mach numbers above
20, over a large wall temperature range.   Large real gas effects
(varying specific heats and dissociation effects) on the calcu-
lated heat-transfer rates and wall shear stresses were encountered
on a slightly blunted cone at Mach number 22 where entropy swal-
lowing was important.   Smaller, but still significant, real gas
effects were found with the same configuration and flight condi-
tions whenever the boundary-layer edge conditions were calculated
using the normal shock entropy.   For a sharp cone with laminar
flow at Mach number 25 and 100,000 ft, perfect gas calculations
were valid within about 13-percent accuracy for heat-transfer
rate or wall shear stress at wall temperatures from 540 to 3,000°R.

AFSC
Arnold AFS Tenn

PREFACE

The work reported herein was conducted by the Arnold Engineering Development Center (AEDC), Air Force Systems Command (AFSC). The results of the research were obtained by ARO, Inc. (a Sverdrup Corporation Company), AEDC Division, operating contractor for the AEDC, AFSC, Arnold Air Force Station, Tennessee, under ARO Project No. V32A-P1A. Mr. Elton Thompson, DOTR, was the Air Force project manager. The manuscript was submitted for publication on November 20, 1978.

The author would like to acknowledge the contributions of Dr. R. Michael Evans of Aerotherm/Acurex Corporation, Mountain View, California (Aerotherm), who has acted as a consultant to AEDC on the BLIMP code and who directed most of the code changes necessary for this project. The contributions of Mr. E. W. Dorrell, ARO, Inc., who has performed most of the programming work at AEDC in connection with the BLIMP code, are also recognized. The turbulence model was incorporated in the Lubard-Helliwell fully viscous shock layer code by Dr. A. W. Mayne, ARO, Inc.

CONTENTS

ILLUSTRATIONS

TABLE

APPENDIX A

1.0 INTRODUCTION

The Aerotherm BLIMP (Boundary Layer Integral Matrix Procedure) boundary-layer code provides numerical solutions of the nonsimilar, multicomponent, laminar or turbulent boundary layer with equilibrium or nonequilibrium chemical systems, unequal diffusion and thermal diffusion coefficients for all species, and a variety of surface boundary conditions including intimate coupling with transient charring — ablation energy and mass balances. The code was originally developed in 1966 (Ref. 1) and has been modified extensively (Refs. 2-8) and used widely since that time. Numerous comparisons have been made of BLIMP boundary-layer calculations with results from other computation schemes and with experimental data (see Refs. 1, 4, and 7, for example). The objective of this report is to make further comparisons at conditions more appropriate to the early portion of a reentry flight (150,000 to 100,000 ft), that is, at altitudes still high enough that ablation and shape change are not important, but low enough that low density effects are also not important. In addition, the investigations reported by Evans (Ref. 7) and Bonnett and Evans (Ref. 8) suggested that the turbulence model in BLIMP might severely overestimate wall heat-transfer rates, and it was desired to study this problem at reentry conditions.

BLIMP calculations were made for a slender blunted and a slender sharp cone configuration at Mach numbers 22 and 25, respectively, an altitude of 100,000 ft, and several wall temperatures, for both laminar and turbulent flow. The results were compared with (1) the fully viscous shock layer method of Lubard and Helliwell (Ref. 9), (2) the boundary-layer program of Mayne and Dyer (Ref. 10), which is based on the boundary-layer solution scheme of Patankar and Spalding (Ref. 11), and (3) the sharp cone boundary-layer solutions of Adams (Ref. 12). For these computations wall heat-transfer rates, wall shear stresses, and the boundary-layer displacement thicknesses and momentum thicknesses were compared. BLIMP predictions of the wall heat-transfer rate were also compared with measurements made during a flight experiment, Reentry F, of a 5-deg half-angle slightly blunted cone which flew at Mach numbers near 20. Laminar, transitional, and turbulent heat-transfer rates were measured during this flight at high Mach number, high total enthalpy, and low ratio of wall temperature to free-stream total temperature conditions (which cannot be duplicated in ground test facilities). The availability of these data provided an opportunity to check the validity of the BLIMP turbulence model at reentry conditions.

2.0 ANALYTIC METHODS

Analytical results from four different numerical flow-field calculation techniques will be given in this report. The main similarities and differences in these techniques will be briefly mentioned here. No attempt was made to predict the transition location for any of the calculations. For the purely analytical results, the location for the onset of transition and the

extent of the transition zone were chosen arbitrarily, but the same for all methods. The BLIMP code was modified so that an exponential scaling of the eddy viscosity in the transition zone could be made in a manner similar to the other calculation schemes (see Ref. 12, p. 19 for details of the exponential scaling of eddy viscosity). For the comparisons with experimental data, the transition locations were deduced from the experiments.

2.1 BLUNT BODIES

Results from three of the numerical flow-field calculation techniques will be presented for the blunt bodies. The Lubard-Helliwell fully viscous shock layer code (Ref. 9) is quite different from the two boundary-layer codes (BLIMP, Ref. 6, and Patankar-Spalding, Ref. 11) in that the equations which are solved are valid in both the viscous and inviscid regions, which eliminates boundary-layer displacement effects and matching problems between the viscous and inviscid regions. That is, the various flow quantities vary smoothly from the wall all the way to the shock, and there is no need to iterate between the viscous and inviscid solutions. The pressure varies continuously across the shock layer so that no assumption of zero normal pressure gradient is necessary — as in the case of the boundary-layer programs. The turbulence modeling in the Lubard-Helliwell code is essentially the same as that in the Patankar-Spalding code. The Lubard-Helliwell calculations assume a perfect gas with a constant specific heat (C_p) in conjunction with the Sutherland viscosity law and Pr = 0.71.

The boundary-layer calculations, BLIMP and Patankar-Spalding, were run with identical inviscid data (pressure distribution and shock shape). The NASA Ames two-dimensional and axisymmetric characteristics solution program (Ref. 13) was used for both perfect and real gas; the blunt body solutions of Aungier (Ref. 14) or Lomax and Inouye (Ref. 15) or Inouye (Ref. 16) were used as the blunt body solutions. The boundary-layer solutions were *not* iterated with the inviscid solution so that there is some mismatch in flow conditions at the edge of the boundary layer between the viscous and inviscid solution. Comparison of the boundary-layer profiles and the characteristics solution profiles with the fully viscous shock layer solution profiles gave estimates of the magnitude of the displacement effects. Both boundary layer calculation methods have a real gas option.

2.2 SHARP BODIES

Although each of the analytical methods could have been used to make calculations for the sharp cones, only the code of Ref. 12 and the BLIMP code (Ref. 6) were used. Both codes execute rapidly on the computer, and a large number of runs could be made quite easily. Results calculated by the Ref. 12 code are well documented, both in Ref. 12 where extensive detailed comparisons were made, and in numerous AEDC-VKF applications since Ref. 12 was published. Generally, the calculations are quite good for laminar, transitional,

and turbulent boundary layers under a wide range of flow and angle-of-attack conditions. Most of the analytic comparisons shown in this report are made at zero degree angle of attack. However, the Reentry F flight vehicle oscillated at small angles of attack (less than 1 deg) during the period when the turbulent data were recorded, so that angle-of-attack effects in the plane of symmetry had to be considered. The Ref. 12 code employs a three-dimensional windward plane-of-symmetry boundary-layer analysis, but an axisymmetric analogy technique had to be used in BLIMP for angle-of-attack effects. A three-dimensional inviscid conical flow analysis was used to determine the pressure and shock shape for both Ref. 12 and BLIMP. The code of Ref. 12 assumes a perfect gas, whereas the BLIMP calculations can also be made with a real gas, i.e., considering caloric imperfections and chemical reactions with multicomponent diffusion.

2.3 TURBULENCE MODELS

The turbulence models in three of the computer codes, the Patankar-Spalding code, the Lubard-Helliwell code, and the Ref. 12 code are essentially the same (except that Ref. 12 has modifications necessary to treat the three-dimensional problem), and are based on recommendations of Escudier (Ref. 17) and of Patankar and Spalding for the variation of mixing length across the boundary layer. All of these models will be referred to here as the Patankar-Spalding model. An additional turbulence model was added to the BLIMP code for this study, the model of Cebeci and Smith (Ref. 18). This model will be referred to as BLIMP/CEBECI or Cebeci-Smith, and the standard BLIMP turbulence model will be called BLIMP/KENDALL or BLIMP turbulence model. The overall formulation of all three turbulence models considered here is quite similar. The turbulent boundary-layer shear stresses are treated using a two-layer, inner-outer model in conjunction with Prandtl's mixing-length hypothesis. For the two-dimensional turbulent boundary layer, the effective shear stress is

$$r = \mu \frac{\partial \overline{u}}{\partial y} - \overline{\rho} \, \overline{u'v'} \tag{1}$$

By adapting Boussinesq's eddy viscosity concept, the Reynolds stress may be represented as

$$- \overline{\rho} \, \overline{u'v'} = \epsilon_m \frac{\partial \overline{u}}{\partial y} \tag{2}$$

7

AEDC-TR-79-6

and the heat transfer as

$$- \overline{\rho}\, \overline{v'h'} = \frac{\epsilon_h}{C_p}\, \frac{\partial \overline{h}}{\partial y} \tag{3}$$

Prandtl's mixing length hypothesis is employed to obtain

$$- \overline{\rho}\, \overline{u'v'} = \overline{\rho}\, \ell^2 \left| \frac{\partial \overline{u}}{\partial y} \right|^2 \tag{4}$$

so that the eddy viscosity is

$$\epsilon_m = \overline{\rho}\, \ell^2 \left| \frac{\partial \overline{u}}{\partial y} \right| \tag{5}$$

Up to this point, all of the turbulence models are the same. Differences in the models arise in the calculation of the mixing length.

2.3.1 The Wall (Inner) Region

The models of Patankar-Spalding and of Cebeci-Smith use an expression originating with Prandtl that in the inner region

$$\frac{d\ell}{dy} = k \tag{6}$$

which has the solution

$$\ell = ky \tag{7}$$

In both these models, the van Driest (Ref. 19) exponential damping of the turbulent part of the shear stress is used, so that the mixing length expression becomes

$$\ell = ky \left[1 - \exp\left(-y^+/A^+\right) \right] \tag{8}$$

where

$$y^+ = y\, \sqrt{\tau_w\, \rho}/\nu \tag{9}$$

8

In the Patankar-Spalding formulation, k is taken as 0.435 and A^+ is taken to be 26.0; whereas in the Cebeci-Smith model, these constants are replaced by functions which account for pressure gradient and mass addition.

The BLIMP/KENDALL model uses an expression based on

$$\frac{d\ell}{dy} \sim (ky - \ell) \tag{10}$$

i.e., the rate of increase of the mixing length with y is proportional to the difference between the value postulated by Prandtl (ky) and its actual value. The proportionality factor in this relation is assumed to be dependent on the local shear stress and the local kinematic viscosity, so that for incompressible flow

$$\frac{d\ell}{dy} = (ky - \ell) \left(\frac{\sqrt{\tau/\rho}}{y_a^+ \nu} \right) \tag{11}$$

where y^+ is a constant (11.823) and k is taken to be 0.44. These constants were obtained by matching predictions in incompressible turbulent boundary layers with and without mass addition (Ref. 20). Physically y^+ is a measure of the thickness of the laminar sublayer. For compressible flow, the wall law is modified so that

$$\frac{d(\rho\ell)}{dy} = \left[k \int_0^y \rho dy - \rho\ell \right] \frac{\sqrt{\tau/\rho}}{y_a^+ \nu} \tag{12}$$

where instead of describing the length scale of a turbulent eddy, the mass of the eddy ($\rho\ell$) is related to the mass available between the wall and point of interest. The constants k and y_a^+ are left at their incompressible values. The above integral-differential equation is solved numerically to obtain the local value of the mixing length (ℓ).

2.3.2 The Outer (Wake) Region

For the Patankar-Spalding model, the mixing length in the outer region is calculated as

$$\ell = \lambda y_\ell \tag{13}$$

where $\lambda = 0.09$ and y_ℓ is the value of y at the point where the velocity in the boundary-layer is 0.99 of the boundary layer outer edge velocity.

For the Cebeci-Smith and BLIMP/KENDALL models, the mixing length is

$$\ell = c\delta_i^* \tag{14}$$

where

$$\delta_1^x = \int_0^\delta \left(1 - \frac{u}{u_e}\right) dy \tag{15}$$

and where c = 0.0168 for the Cebeci-Smith model and 0.0180 for the BLIMP/KENDALL model. Furthermore, the eddy viscosity is taken to be a constant in the wake region for both models

$$\epsilon_m = c u_e \delta_i^x ; \quad \text{or} \quad (= \ell V_t) \tag{16}$$

where V_t is the turbulent velocity and is taken equal to u_e.

2.3.3 General

The end of the inner region and the beginning of the outer region is calculated as follows for all three turbulence models. From the wall outward, the expression for the inner eddy viscosity is used until $(\epsilon_m)_{inner} = (\epsilon_m)_{outer}$ from which point the outer viscosity is used.

The turbulent Prandtl number is defined as

$$Pr_t = \frac{C_p \epsilon_m}{\epsilon_h} \tag{17}$$

and is used to determine the value of eddy thermal conductivity which is needed in the energy equation. The turbulent Prandtl number was taken equal to 0.9 for the Patankar-Spalding and the BLIMP/KENDALL turbulence models but was a variable for the Cebeci-Smith model. The reader is referred to Ref. 7 for details on the way this varying turbulent Prandtl number is calculated in BLIMP. For the conditions reported here (where the Cebeci-Smith model was used), the turbulent Prandtl number varied from 1.4 at the wall to 0.90 at the edge and, at some downstream stations, was 0.90 across the whole boundary layer.

2.4 CALCULATION TECHNIQUES

2.4.1 Patankar-Spalding (Ref. 11)

The boundary-layer equations expressing the conservation of mass, momentum, and energy are transformed into a normalized von Mises coordinate system and solved using a marching, implicit finite difference procedure. The code can handle perfect gas cases or real gas cases, where the real gas data are based on the correlation formulas of Cohen (Ref. 21).

2.4.2 Lubard-Helliwell (Ref. 9)

An approximate system of equations is derived from the steady-state Navier-Stokes equations by assuming the viscous, streamwise derivative terms are small compared with the viscous normal and circumferential derivatives. These equations are valid in both the viscous and inviscid regions including the circumferential separation zone which develops on the leeward side at the higher angles of attack. An implicit differencing technique with iteration is used to solve the resulting three-dimensional parabolic equations. The AEDC version of this code has been modified by Mayne (Ref. 22) to consider the case of flow over blunt biconics and more recently to consider turbulent flow. The code does not handle real gases.

2.4.3 Three-Dimensional Windward Plane of Symmetry (Ref. 12)

The code uses a three-dimensional windward plane-of-symmetry laminar, transitional, and turbulent boundary layer analysis coupled with a three-dimensional inviscid conical flow analysis for a sharp cone at angle of attack. The boundary-layer equations are numerically integrated using an implicit finite-difference technique which marches along the windward streamline starting at the apex of the cone with a laminar similar solution. The code employs perfect gas assumptions.

2.4.4 BLIMP (Ref. 6)

The BLIMP (Boundary Layer Integral Matrix Procedure) code combines features of the general integral relations approach with those of matrix solution techniques. Smooth functions (cubic spline functions, or quadratics) are chosen to relate the principal dependent variables to their derivatives. This enables the attainment of an accurate solution with relatively few entries into the conservation equations. The entire solution is treated as a set of simultaneous nonlinear algebraic equations. The formulation considers unequal diffusion and thermal diffusion coefficients for all species through a bifurcation approximation for binary diffusion coefficients. The multicomponent viscosity and thermal conductivity of the mixture are determined by use of Sutherland-Wassiljewa-type approximations.

For the calculations in this report, a ten-species air model consisting of O_2, N_2, O, N, NO, A, N^+, O^+, NO^+, and e- was used for all real gas calculations; details are given in Appendix A. Real gas transport properties were based on the diffusion factors given in Appendix A. The gas was taken to be in chemical equilibrium, with unequal diffusion coefficients and thermal diffusion considered. Fifteen nodal points (the maximum dimension of the AEDC program) were used in all calculations to describe variations across the boundary layer. The stretching parameter was determined using a constraint on the total

enthalpy for all calculations. For perfect gas calculations, the Sutherland viscosity equation (Ref. 23) was used with $C_p = 0.23989$ btu/lb and $Pr = 0.71$.

3.0 ANALYTIC RESULTS

The general objective of the analytic study was to compare BLIMP boundary-layer calculations with calculations from several often-used, well-documented flow-field solution methods available at the AEDC-VKF for conditions representative of the early portion of typical reentry flights (150,000 to 100,000 ft). While the BLIMP program is a sophisticated code capable of treating ablating flows with chemical reactions (equilibrium or nonequilibrium), this work is concerned only with simple nonablating-type flows in chemical equilibrium. Calculations were made on both sharp and slightly blunted cones at high Mach numbers. Many of the calculations presented assume that the fluid is a perfect gas with $\gamma = 1.4$. These perfect gas results allow a direct evaluation of the capability of the BLIMP numerical technique to produce an answer consistent with other codes, because the gas thermodynamic properties and transport properties can be calculated in exactly the same way in all the computer codes. Comparisons are then made of these perfect gas calculations with real gas solutions (varying specific heats and equilibrium chemical reactions with diffusing species) to assess the real gas effects. The main quantities of interest here are the wall heat-transfer rates and wall shear stresses. Some comparisons are made of the boundary-layer integral quantities (displacement thickness, momentum thickness) for the sharp cone solutions, but the AEDC version of the BLIMP code has incorrect definitions of the boundary-layer integral quantities whenever entropy swallowing is important; therefore, these comparisons could not be made for the blunt cone solutions. Attention is also focused on the turbulence model in the BLIMP program because Evans (Ref. 7) and Bonnett and Evans (Ref. 8) pointed out that the Kendall model used in BLIMP could overpredict measured heat-transfer rates by a factor as large as two whenever there were large property variations across the boundary layer, i.e., high values of T_e/T_w (see Fig. 3 of Ref. 8, for example).

3.1 SHARP CONE CALCULATIONS

Both the BLIMP code (Ref. 6) and the code of Ref. 12 were used to make a series of boundary-layer calculations on a 10-ft-long, 5-deg half-angle sharp cone at Mach number 25 and an altitude of 100,000 ft. Calculations were made for both laminar flow, and for turbulent flow with a transition onset location of $S = 2$ ft. The transition zone extended over a length of 2 ft, so that fully turbulent flow occurred at $S = 4$ ft. Calculations were made for three different wall temperatures: 540, 3,000, and 9,000°R (while 9,000°R is not a practical nonablating temperature, it was chosen as an extreme upper limit to study real gas effects from a theoretical point of view). BLIMP calculations were made for both real gas

data, though the differences are larger. Integrated values of the skin friction (in coefficient form) over the 10-ft length body are given in Fig. 4, and again the laminar comparisons are excellent. The turbulent integrated skin friction results are a reflection of the integration of a local skin friction variation similar to the heat-transfer rate distributions of Fig. 1. At the low wall temperature, the BLIMP results are 9.5 percent higher than the Ref. 12 code results, and this is consistent with the results shown in Fig. 1a. There is better agreement at $T_w = 3,000°R$ as implied by Fig. 1b, and a similar analogy with Fig. 1c applies.

Real gas effects on the calculation of wall shear stresses and wall heat-transfer rates are summarized in Figs. 5 and 6 for this sharp cone configuration at $M_\infty = 25$ and 100,000 ft. These results were obtained using the BLIMP boundary-layer code, and the BLIMP/KENDALL turbulence model was used for the turbulent calculations. The wall shear stresses in laminar flow can be determined within about 13 percent from perfect gas calculations at the T_w values shown, with the real gas shear stresses always above the perfect gas values. This is also true at $T_w = 3,000°R$ though the data are not shown. The 540°R wall case is of interest because at this low temperature the perfect gas and real gas transport properties are almost equal ($\mu_{real}/\mu_{perfect} = 1.005$) and there is no diffusion directly to the wall. However, in this high enthalpy flow, species diffusion in the boundary layer at points away from the wall have altered the velocity and temperature profiles and affected the wall shear stresses and heat-transfer rates by 13 percent. At the lowest wall temperature, the turbulent shear stress results are more sensitive to real gas effects than the laminar shear stress results. The real gas turbulent shear stresses are up to 30 percent higher than the perfect gas shear stresses in the fully turbulent regime at $T_w = 540°R$.

The real gas laminar heat-transfer rates are about 13 percent above the perfect gas solutions at the lower temperatures (Fig. 6, $T_w = 3,000°R$ not shown), but at $T_w = 9,000°R$ the real gas calculations are 30 percent *lower* than the perfect gas calculations. Thus, there is a wall temperature range (540°R < T_w < 3,000°R) in which perfect gas calculations of the laminar shear stress and heat-transfer rate are generally within 13 percent of the real gas values, but there are not enough calculations here to clearly define the range or the accuracies. Note that the wall temperature of 9,000°R is unrealistically high for a nonablating condition, and the calculation is shown only to consider an extreme case theoretically. Considerably more real gas effects are shown for the turbulent flow heat-transfer rates. The real gas heat-transfer rates are up to 27 percent higher than the perfect gas heat-transfer rates in the fully turbulent regime at T_w of 540°R.

3.2 BLUNT CONE CALCULATIONS

The BLIMP, Patankar-Spalding, and Lubard-Helliwell fully viscous shock layer codes were used to calculate the flow over a slightly blunted 7-deg half-angle cone at Mach number 22 at an altitude of 100,000 ft. The body was 9-1/2 ft long and had a nose radius of 0.08333 ft. Both laminar and turbulent flows were calculated and instantaneous transition at the sphere-cone tangent point was assumed. BLIMP calculations were made for both real and perfect gas at several wall temperatures namely, 540, 3,000, and 9,000°R (again, the 9,000°R temperature is not a practical nonablating temperature, but was chosen as an extreme upper limit to study real gas effects from a theoretical point of view). Several Patankar-Spalding runs were made for the same three temperatures for a perfect gas; and real gas calculations (both laminar and turbulent) were made at a temperature of 540°R. The viscous shock layer program is limited to a perfect gas assumption, and laminar and turbulent calculations were made only at a wall temperature of 540°R. These results are given in Figs. 7 through 16.

Laminar, perfect gas, heat-transfer rates in the stagnation and spherical region of the body are compared in Fig. 7 for the three methods. Very good agreement is indicated at both wall temperatures. This good agreement is also obtained on the afterbody for the perfect gas laminar solutions (see Figs. 8a, b, and c). The boundary-layer solutions agree remarkably well; and at least part of the difference between the viscous shock-layer solution and the boundary-layer solutions (see Fig. 8a) may be attributed to viscous interaction effects that are unaccounted for in the boundary-layer solutions.

The turbulent perfect gas solutions at $T_w = 540°R$ (Fig. 8a) show a 40-percent difference in heat-transfer rate between the BLIMP code calculations (Kendall turbulence model) compared with both the Patankar-Spalding and the Lubard-Helliwell code calculations. It is noted again that the turbulence model in the Lubard-Helliwell code is virtually the same as that in the Patankar-Spalding code so that comparable results (excluding boundary-layer displacement effects) are expected from the codes. The difference between BLIMP and the other methods is in the same direction (an overprediction) as the overprediction of the experimental data shown by Bonnett and Evans in Ref. 8 when there were large property variations across the boundary layer. Notice that, at the higher wall temperatures (Figs. 8b and c), the BLIMP/KENDALL calculations approach the other results and are in good agreement at $T_w = 9,000°R$.

To further investigate the above effects, it was decided to incorporate another turbulence model in the AEDC version of BLIMP. The Cebeci-Smith turbulence model (Ref. 18) had previously been used in BLIMP by Evans (Ref. 7) and was provided to AEDC under a

consulting contract with Aerotherm. Results from BLIMP calculations with the Cebeci-Smith model are shown in Fig. 8 and are in good agreement with the results from the other codes even at the lowest wall temperature. Even though these theoretical results are not conclusive, it seems likely that the BLIMP/KENDALL model overpredicts the heat-transfer rate.

A graph of the wall shear stress variation calculated by the various codes for the T_w = 540°R case is given in Fig. 9. The data look very similar to the heat-transfer rate comparisons of Fig. 8a; again there is excellent agreement of the laminar results, and again the BLIMP/KENDALL turbulent shear stress results are higher than the shear stresses from the other codes. Once again the BLIMP/CEBECI results are much closer to the calculations from the other codes.

A comparison is made in Fig. 10 of the pressure distributions along the body as calculated by the inviscid characteristics solution with that calculated by the viscous shock-layer program. Viscous interaction effects on the pressure are at most 10 percent (at an S/R ≈ 50).

Observation of the velocity profiles across the shock layer for this entropy swallowing (blunt nose) case will demonstrate how well the various boundary-layer flow quantities match into the inviscid solution (no iteration was performed) and how they compare with the continuously varying quantities of the viscous shock-layer solution. Velocity distributions for the laminar boundary layer at S = 6.67 ft are presented in Fig. 11. The inviscid wall velocity is 18,050 ft/sec, and proceeding from the wall the inviscid velocity rapidly approaches 21,600 ft/sec. The boundary-layer velocity profiles from BLIMP and Patankar-Spalding are in good agreement, and at this station, the edge velocity has just about reached its maximum value. The fully viscous shock-layer (Lubard-Helliwell) profiles fair smoothly into the inviscid velocities. The viscous layer shock is further from the body than the inviscid characteristics solution shock because of viscous interaction effects.

Velocity and total enthalpy distributions are plotted across the shock layer for the turbulent boundary layer at S = 7.18 ft in Figs. 12 and 13. The turbulent boundary layer is, of course, much thicker than the laminar one, and the edge velocity is reached further out on the inviscid velocity curve where the profile is flat. The BLIMP/CEBECI profiles agree well with the Patankar-Spalding profiles.

Real gas effects on the afterbody heat-transfer rate calculations are presented in Fig. 14. Entropy layer swallowing results from the Patankar-Spalding code and the BLIMP code are compared in Fig. 14a, and BLIMP calculations made both with and without entropy swallowing are given in Figs. 14b and c, for turbulent and laminar flow, respectively.

Figure 14a shows that the perfect gas assumption for this Mach number 22, 100,000-ft altitude case results in a considerable underprediction of the afterbody heat-transfer rates, especially for turbulent flow. The real gas calculations are as much as 70 percent above the perfect gas calculations for the turbulent boundary layer (using the BLIMP/CEBECI calculation). Considerably less effect is indicated for the laminar flow boundary layer - a maximum of 13 percent for the BLIMP results and 9 percent for the Patankar-Spalding results. Note that for clarity only one line is shown for the perfect gas laminar calculations from both the BLIMP and Patankar-Spalding codes since these calculations were shown to be practically the same in Fig. 8a. Similarly, there is one line given for both the perfect gas turbulent Patankar-Spalding calculation and the perfect gas, turbulent BLIMP/CEBECI calculation (see Fig. 8a).

The real gas laminar calculations of BLIMP and Patankar-Spalding (Fig. 14a) do not agree as well as the perfect gas calculations (Fig. 8a) apparently because of the different thermodynamic and transport properties in the codes. There is as much as an 8-percent difference in the calculations. The real gas turbulent boundary-layer heat-transfer rate calculations made using the BLIMP/KENDALL turbulence model gives results considerably higher than the Patankar-Spalding results; and the BLIMP/CEBECI turbulence model results are in much better agreement with the Patankar-Spalding calculations. These trends are consistent with the perfect gas results.

The graphs in Figs. 14b and c give a breakdown of real gas effects for calculations made with and without entropy swallowing. The turbulent calculations in Fig. 14b were made using the BLIMP/CEBECI turbulence model. Laminar calculations are given in Fig. 14c. A very pronounced effect of entropy swallowing is shown for the turbulent boundary layer in Fig. 14b. An 80-percent increase in heat-transfer rate is indicated at some body stations when real gas properties are used and a 50-percent increase when perfect gas assumptions are made. Also, by comparing real gas and perfect gas calculations, it may be seen that real gas effects are considerably higher when entropy swallowing is included in the calculation. Real gas effects are much smaller for the laminar boundary layer as shown in Fig. 14c.

The increase in afterbody heat-transfer rates due to real gas effects shown previously in Fig. 14 are due in part to inviscid real gas effects. The real gas pressures are somewhat higher than the corresponding perfect gas pressures (Fig. 15), and the entropy change across the shock is considerably larger for the real gas (Fig. 16) (especially near the stagnation point) and would have some effect on the entropy swallowing results of Fig. 14.

A summary of real gas effects on the wall heat-transfer rates and wall shear stresses at S = 7.18 ft for various wall temperatures and for both laminar and turbulent boundary layers

is given in Table 1 (based on BLIMP/KENDALL calculations). At the lower wall temperatures, the real gas heat-transfer rates and wall shear stresses are higher than the perfect gas values, but at $T_w = 9,000°R$, the equilibrium chemical reactions with molecular diffusion take over, and the real gas heat-transfer rate is less than the perfect gas rate. This higher temperature is not a practical nonablating temperature and was chosen as a theoretical extreme for the perfect gas comparisons. Real gas effects in the turbulent cases would have been larger if BLIMP/CEBECI calculations had been used, but these calculations were not available at all wall temperatures.

Table 1. Summary of Real Gas Effects at S = 7.18 ft on a Blunted 7-deg Half-Angle Cone at Mach Number 22 and 100,000-ft Altitude from BLIMP/KENDALL Calculations ($S/R_H = 86.16$)

	Laminar Flow			Turbulent Flow		
$T_w = 540°R$	Real	Perfect	Real/ Perfect	Real	Perfect	Real/ Perfect
$\dot{q}$ (Btu/ft²-sec)	70.0	63.8	1.097	350.7	286.7	1.223
τ_w (lb/ft²)	3.77	3.62	1.041	22.08	17.95	1.230
$T_w = 3,000°R$						
$\dot{q}$ (Btu/ft²-sec)	60.4	56.6	1.067	293.7	226.6	1.296
τ_w (lb/ft²)	3.64	3.42	1.064	20.59	15.04	1.369
$T_w = 9,000°R$						
$\dot{q}$ (Btu/ft²-sec)	25.4	42.4	0.599	103.4	145.6	0.710
τ_w (lb/ft²)	3.14	3.12	1.008	14.23	11.60	1.227

4.0 COMPARISON OF ANALYTIC RESULTS WITH HEAT-TRANSFER RATES MEASURED DURING THE REENTRY F FLIGHT EXPERIMENTS

High-quality laminar, transitional, and turbulent heat-transfer rate data were measured during the Reentry F flight at a Mach number of 20 on a 5-deg half-angle cone 13 ft long with an initial nose tip radius of 0.10 in. This flight provided needed experimental data in regimes of simultaneous high Mach number, high Reynolds number, high total enthalpy, and low ratio of wall-to-total temperature. In the altitude range from 100,000 to 60,000 ft, data were obtained at Mach number 20, free-stream Reynolds numbers per foot of 2×10^6 to 16×10^6 and total enthalpy of 7,900 to 7,300 Btu/lb.

18

4.1 THE REENTRY F FLIGHT

The Reentry F flight was conducted from Wallops Station, Virginia, on April 22, 1968. In planning the flight, care was taken to ensure that the test and environmental data would be of high quality and would be as free as possible from complicating factors such as pressure gradients and angle of attack. To limit nose bluntness effects, the initial nose tip radius was very small (0.1 in.). The primary structure was a 0.60-in.-thick beryllium cone with an ATJ graphite nose tip. The primary measurement was the surface convective heat-transfer rate, although pressure distributions were also measured on the cone. Details concerning the instrumentation and other data required to analyze the flight are given in Refs. 24 through 26.

Reentry F data provide an excellent opportunity to compare analytic results, obtained from BLIMP (Ref. 6) and from Ref. 12, with flight data in the turbulent regime. Transition was first detected on the spacecraft at an altitude slightly higher than 100,000 ft, and it was necessary to examine data at lower altitudes so that there would be a reasonable length of fully turbulent flow on the body. At altitudes of 87,000 ft and below, the spacecraft began a small pitch/yaw motion which created surface distortion because of temperature differences around the body. The results of a theoretical calculation of the body shape at various altitudes is given in Ref. 24. The forward portion of the spacecraft distorted more than the rear, with the leeward side of the body (0-deg ray) and the 270-deg ray assuming a concave shape. For the present comparison, flight data at an altitude of 77,000 ft are shown, where the body distortion was still relatively small (about 0.1 deg at a point 10 in. from the nose, and less downstream) and the fully turbulent region on the body was long enough to have several heat-transfer rate measurements for comparison. At this altitude, the spacecraft was at an angle of attack of 0.35 deg, which was considered in the theoretical calculations.

An analysis of the nosetip performance is presented in Ref. 24, which considered both the thermochemical oxidation process with equilibrium chemistry, and also mechanical erosion effects (using ground test data). The analysis shows that the nosetip had a hemispherical radius at the stagnation point of approximately 0.16 in. at 77,000 ft. For the theoretical calculations presented below, the nosetip was considered to be sharp since the flight measurements under consideration here were measured at stations at least 2-½ ft downstream of the nose ($S/R_N \approx 190$).

4.2 THEORETICAL ANALYSIS AND COMPARISON WITH FLIGHT DATA

Two boundary-layer codes were used to analyze the Reentry F flights - BLIMP (Ref. 6) and the Ref. 12 Code (Adams). The Ref. 12 code uses a three-dimensional windward plane

of symmetry analysis for a sharp cone at incidence, and so can be directly applied to calculating the Reentry F flow on the windward side at angle of attack. An axisymmetric analogy approach (Ref. 27) had to be used with BLIMP because it is a two-dimensional boundary-layer code. The approach used was to calculate a spreading factor (h) for the sharp cone as (from Eq. (34) of Ref. 27)

$$h = r_0 \left(Z/Z_0\right)^{\left(1 - \frac{k}{Tan\,\theta_c}\right)}$$ (18)

where

$$k = \frac{1}{u} \frac{\partial w}{\partial \phi}$$ (19)

and where the k was determined from the tables of Jones (Ref. 28). Also

$$r_0 = Z_0 \, Tan\,\theta_c$$ (20)

and Z_0 was taken as an arbitrary small number; Z is the distance along the body axis measured from the cone apex, and θ_c is the cone half-angle.

The spreading factors are entered into the boundary-layer program just as the axisymmetric radii are usually entered, along with the correct pressure for the cone at angle of attack, and with this input, a usual two-dimensional calculation is made.

Inviscid edge conditions for both BLIMP calculations and the Ref. 12 calculations were determined using the Jones tables (Ref. 28) which are based on an inviscid analysis of a conical flow field about a sharp cone at incidence for a perfect gas. The validity of this approach is indicated in Fig. 17 where the sharp cone inviscid solutions are compared with the measured pressure data of Reentry F. Good agreement is shown for both the windward and leeward sides at 77,000 ft (α = 0.35 deg).

A comparison of the analytic calculations and the flight measurements of the windward and leeward heat-transfer rates at 77,000-ft altitude is given in Fig. 18. The BLIMP calculations make use of real gas properties, while the Ref. 12 code uses perfect gas properties. The BLIMP/CEBECI calculations and the calculations of Ref. 12 are in very good agreement in the fully turbulent region on the windward side, and both calculations represent a good approximation of the flight data. BLIMP/KENDALL turbulent heating calculations are from 10 to 30 percent higher than the flight data and the other calculations.

The BLIMP/CEBECI calculations agree well with the flight data on both the leeward and windward sides, and in both the laminar and turbulent regime; except that the two "laminar" data points on the windward side are considerably underpredicted (about 35 percent). It appears that the flow at S = 4.35 ft may be transitional rather than laminar and that the transition zone is not represented properly in BLIMP for this flight case.

In conclusion, surprisingly good agreement in the fully turbulent region has been shown between reentry vehicle heat-transfer measurements and the perfect gas theory of Ref. 12 and the real gas BLIMP theory using the Cebeci-Smith turbulence model. BLIMP code calculations using the standard Kendall turbulence model appear to overpredict heat-transfer rates at these cold wall conditions.

5.0 CONCLUDING REMARKS

Comparisons of BLIMP calculations with flight data and with the sophisticated flow-field calculation techniques of the Lubard-Helliwell fully viscous shock-layer code, the Patankar-Spalding boundary-layer code, and the Adams three-dimensional windward plane of symmetry sharp cone code indicate the following:

1. The Kendall turbulence model in the BLIMP code overpredicts the heat-transfer rates and wall shear stresses for reentry conditions and the lower wall temperatures. The BLIMP code with the Cebeci-Smith turbulence model provides improved calculations, and this turbulence model should be substituted for the Kendall model. These results corroborate the findings of Evans (Ref. 7) who made comparisons for rocket nozzle flows, and other ground test facility data.

2. Both BLIMP/CEBECI and the Adams code provided results which are in good agreement with the in-flight measured heat-transfer rates of the Reentry F flight in the fully turbulent region.

3. BLIMP calculations under laminar, perfect gas conditions - where the thermodynamic and transport properties were identical - compared extremely well with the other calculation methods for both sharp and slightly blunted cones at Mach numbers above 20 over a large wall temperature range (540 to 9,000°R).

4. Large real gas effects on the calculated heat-transfer rates and wall shear stresses for a slightly blunted cone at Mach number 22 were shown, especially when entropy swallowing effects were considered.

21

5. There is a range of wall temperatures (approximately 540 to 3,000°R at least, but not clearly defined here) where perfect gas calculations provide acceptable heat-transfer rate or wall shear stress values for a sharp cone with laminar flow at Mach number 25 and 100,000-ft altitude.

REFERENCES

1. Bartlett, E. P. and Kendall, R. M. "An Analysis of the Coupled Chemically Reacting Boundary Layer and Charring Ablator, Part III, Nonsimilar Solution of the Multicomponent Laminar Boundary Layer by an Integral Matrix Method." NASA CR-1062, Aerotherm Report 66-7, June 1968.

2. Anderson, L. W. and Kendall, R. M. "A Nonsimilar Solution for Multicomponent Reacting Laminar and Turbulent Boundary Layer Flows Including Transverse Curvature." AFWL TR-69-106, March 1970.

3. Grose, R. D. and Kendall, R. M. "A Nonsimilar Solution for Laminar and Turbulent Boundary Layer Flows Including Entropy Layers and Transverse Curvature." NASA CR-73481, Aerotherm Report 70-14, June 1970.

4. Anderson, L. W. and Morse, H. L. "A Turbulent Model Study for the Multicomponent Nonsimilar Turbulent Boundary Layer Program." AFWL TR-71-57, October 1971.

5. Tong, H. "Nonequilibrium Chemistry Boundary Layer Integral Matrix Procedure." Aerotherm Report UM-73-37, Part I, July 1973.

6. Evans, R. M. "User's Manual-Boundary Layer Integral Matrix Procedure, Including Gas Phase Kinetics - KBLIMPA." Aerotherm UM 75-62, March 1975.

7. Evans, R. M. "JANNAF Boundary Layer Integral Matrix Procedure." Aerotherm Final Report 75-152, July 1975.

8. Bonnett, W. S. and Evans, R. M. "Boundary Layer Integral Matrix Procedure: Verification of Models." Aerotherm Final Report 77-239, April 1977.

9. Lubard, S. C. and Helliwell, W. S. "Calculation of the Flow on a Cone at High Angle of Attack." *AIAA Journal*, Vol 12, No. 7, July 1974, pp. 965-974.

10. Mayne, A. W. and Dyer, D. F. "Comparisons of Theory and Experiment for Turbulent Boundary Layers on Simple Shapes at Hypersonic Conditions." *Proceedings of the 1970 Heat Transfer and Fluid Mechanics Institute*, Stanford University Press, June 1970, pp. 168-188.

11. Patankar, S. V. and Spalding, D. B. *Heat and Mass Transfer in Boundary Layers*. CRC Press, Cleveland, Ohio, 1968.

12. Adams, J. C., Jr. "Implicit Finite-Difference Analysis of Compressible Laminar, Transitional, and Turbulent Boundary Layers along the Windward Streamline of a Sharp Cone at Incidence." AEDC-TR-71-235 (AD734535), December 1971.

13. Inouye, M., Rakich, J. V., and Lomax, H. "A Description of Numerical Methods and Computer Programs for Two-Dimensional and Axisymmetric Supersonic Flow over Blunt-Nosed and Flared Bodies." NASA TN D-2970, August 1965.

14. Aungier, R. H. "A Computational Method for Exact, Direct, and Unified Solutions for Axisymmetric Flow over Blunt Bodies of Arbitrary Shape (PROGRAM BLUNT)." AFWL-TR-70-16, July 1970.

15. Lomax, H. and Inouye, M. "Numerical Analysis of Flow Properties about Blunt Bodies Moving at Supersonic Speeds in an Equilibrium Gas." NASA TR R-204, July 1964.

16. Inouye, M. "Blunt Body Solutions for Spheres and Ellipsoids in Equilibrium Gas Mixtures." NASA TN D-2780, May 1965.

17. Escudier, M. P. "The Distribution of the Mixing Length in Turbulent Flows near Walls." Mechanical Engineering Department Report TWF/TN/1, Imperial College, London, March 1965.

18. Cebeci, T. and Smith, A.M.O. "A Finite Difference Method for Calculating Compressible Laminar and Turbulent Boundary Layers." ASME Paper No. 70-FE-A, presented at ASME Fluids Engineering, Heat Transfer, and Lubrication Conference, Detroit, Michigan, May 24-27, 1970.

19. van Driest, E. R. "On Turbulent Flow near a Wall." *Journal Aerospace Science*, Vol. 23, No. 11, November 1956, pp. 1007-1011, 1036.

20. Kendall, R. M., Rubesin, M. W., Dahn, T. J., and Mendenhall, M. R. "Mass, Momentum, and Heat Transfer within a Turbulent Boundary Layer with Foreign Gas Mass Transfer at the Surface, Part 1 - Constant Fluid Properties." Final Report No. 111, Vidya/Itek Corporation, February 1964.

21. Cohen, N. B. "Correlation Formulas and Tables of Density and Some Transport Properties of Equilibrium Dissociating Air for Use in Solutions of the Boundary Layer Equations." NASA TN D-194, February 1960.

22. Mayne, A. W. "Calculation of the Laminar Viscous Shock Layer on a Blunt Biconic Body at Incidence to Supersonic and Hypersonic Flow." AEDC-TR-76-123 (ADA033225), December 1976.

23. Ames Research Staff. "Equations, Tables, and Charts for Compressible Flow." NACA TR 1135, 1953.

24. Carter, H. S., Raper, J. L., Hinson, W. F., and Morris, W. D. "Basic Measurements from a Turbulent-Heating Flight Experiment on a 5-deg Half-Angle Cone at Mach 20 (REENTRY F)." NASA TM X-2308, September 1971.

25. Wright, R. L. and Zoby, E. V. "Flight Measurements of Boundary Layer Transition on a 5-deg Half-Angle Cone at a Free Stream Mach Number of 20 (REENTRY F)." NASA TM X-2253, May 1971.

26. Zoby, E. V. and Rumsey, C. B. "Analysis of Free-Flight Laminar, Transitional, and Turbulent Heat-Transfer Results at Free-Stream Mach Numbers near 20 (REENTRY F)." NASA TM X-2335, September 1971.

27. Rakich, J. V. and Mateer, G. G. "Calculation of Metric Coefficients for Streamline Coordinates." *AIAA Journal*, Vol. 10, No. 11, November 1972, pp. 1538-1540.

28. Jones, D. J. "Tables of Inviscid Supersonic Flow about Circular Cones at Incidence, γ = 1.4." AGARDograph 137/Part I, November 1969.

29. Deblaye, C. and Bartlett, E. P. "An Evaluation of Thermodynamic and Transport Properties for Use in the BLIMP Nonsimilar Multicomponent Boundary Layer Program." Aerotherm Final Report 69-53, July 1969.

30. Powars, C. A. and Kendall, R. M. "User's Manual - Aerotherm Chemical Equilibrium (ACE) Computer Program." Aerotherm UM 69-7, May 1969.

31. Brahinsky, H. S. and Neel, C. A. "Tables of Equilibrium Thermodynamic Properties of Air." AEDC-TR-69-89, Vols. I-IV (AD686409, AD686410, AD687092, and AD686411, respectively), April 1969.

32. Hilsenrath, J. and Klein, M. "Tables of Thermodynamic Properties of Air in Chemical Equilibrium including Second Virial Correction from 1500°K to 15,000°K." AEDC-TR-65-58 (AD612301), March 1965.

33. Yos, J. M. "Transport Properties of Nitrogen, Hydrogen, Oxygen, and Air to 30,000°K." AVCO RAD-TM-63-7, March 1963.

34. Feigenbutz, L. V. and Solum, E. "Thermodynamic Properties of Air." BUORD Report ERR-SD-005, April 1960.

35. Predvoditelev, A. S. "Table of Thermodynamic Functions of Air, 6,000° to 12,000°K and 0.001 to 1,000 atm." Translated and published by Associated Technical Services, Glen Ridge, N. J. 1962.

36. Hansen, C. F. "Approximations for the Thermodynamic and Transport Properties of High-Temperature Air." NASA TR R-50, 1959.
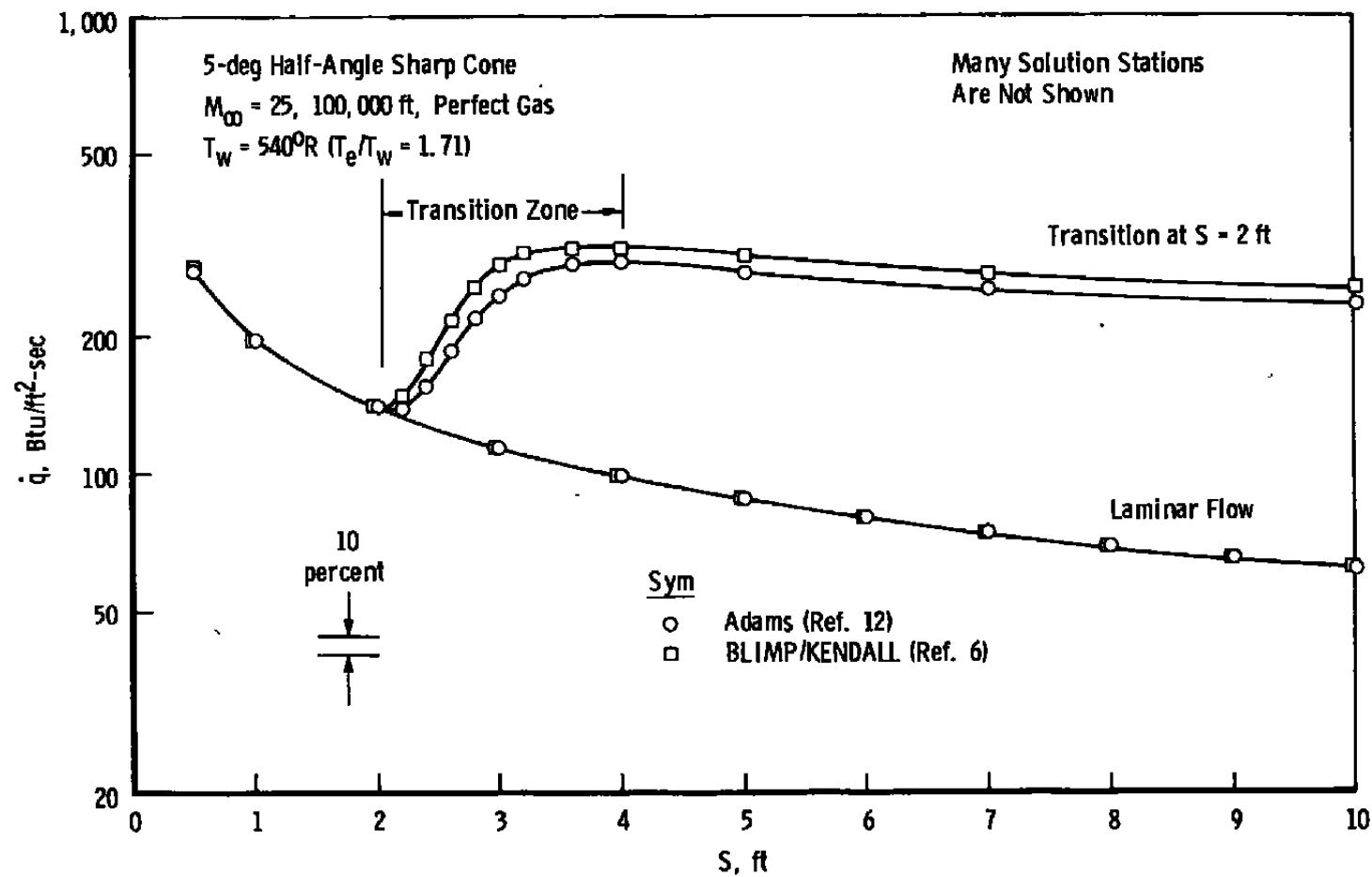
a. $T_w = 540°R$

Figure 1. Calculation of the wall-heat-transfer rate to the surface of a sharp cone at reentry conditions from two boundary-layer solution methods.
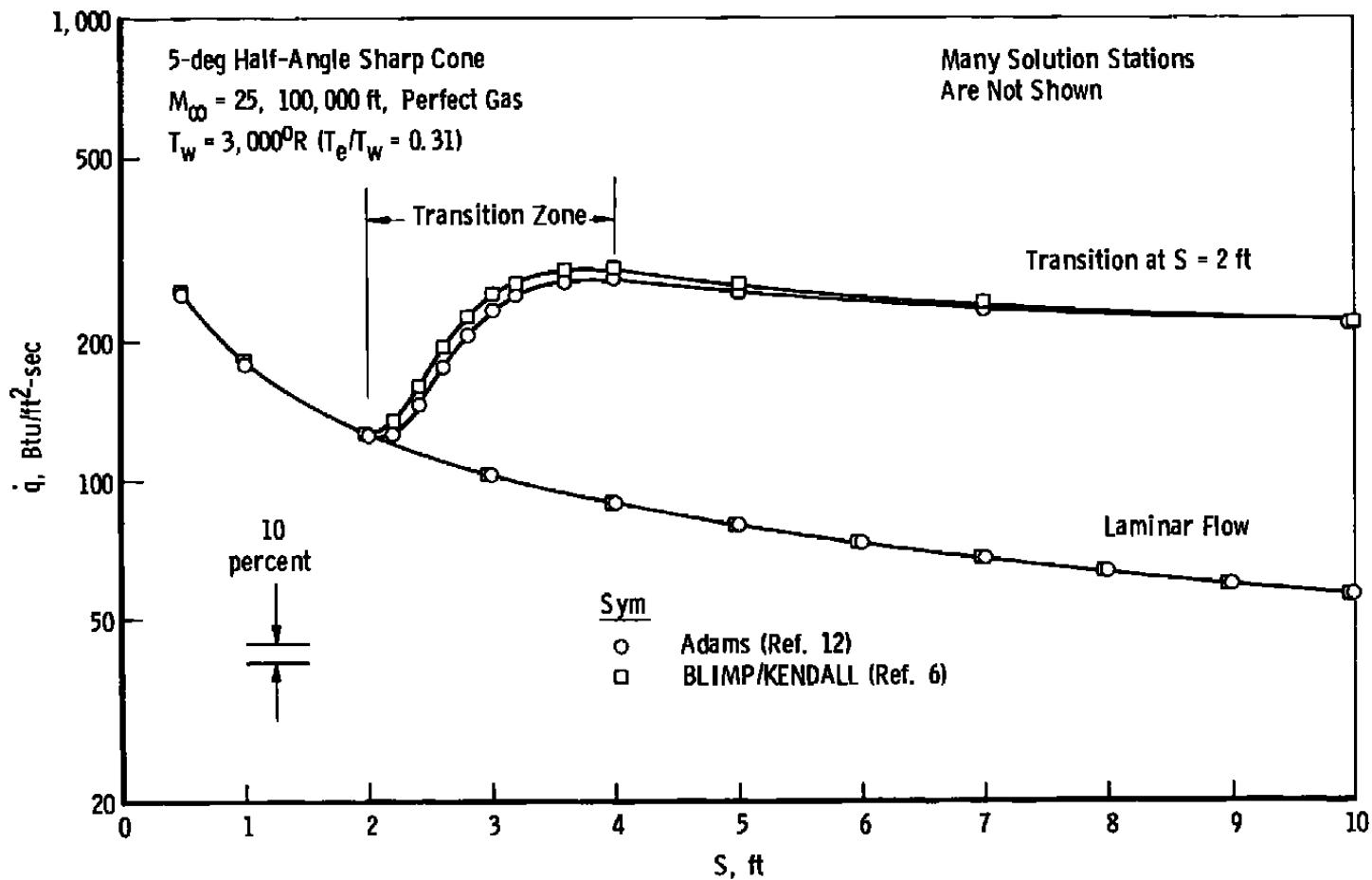
b. $T_w = 3,000\,°R$

Figure 1. Continued.
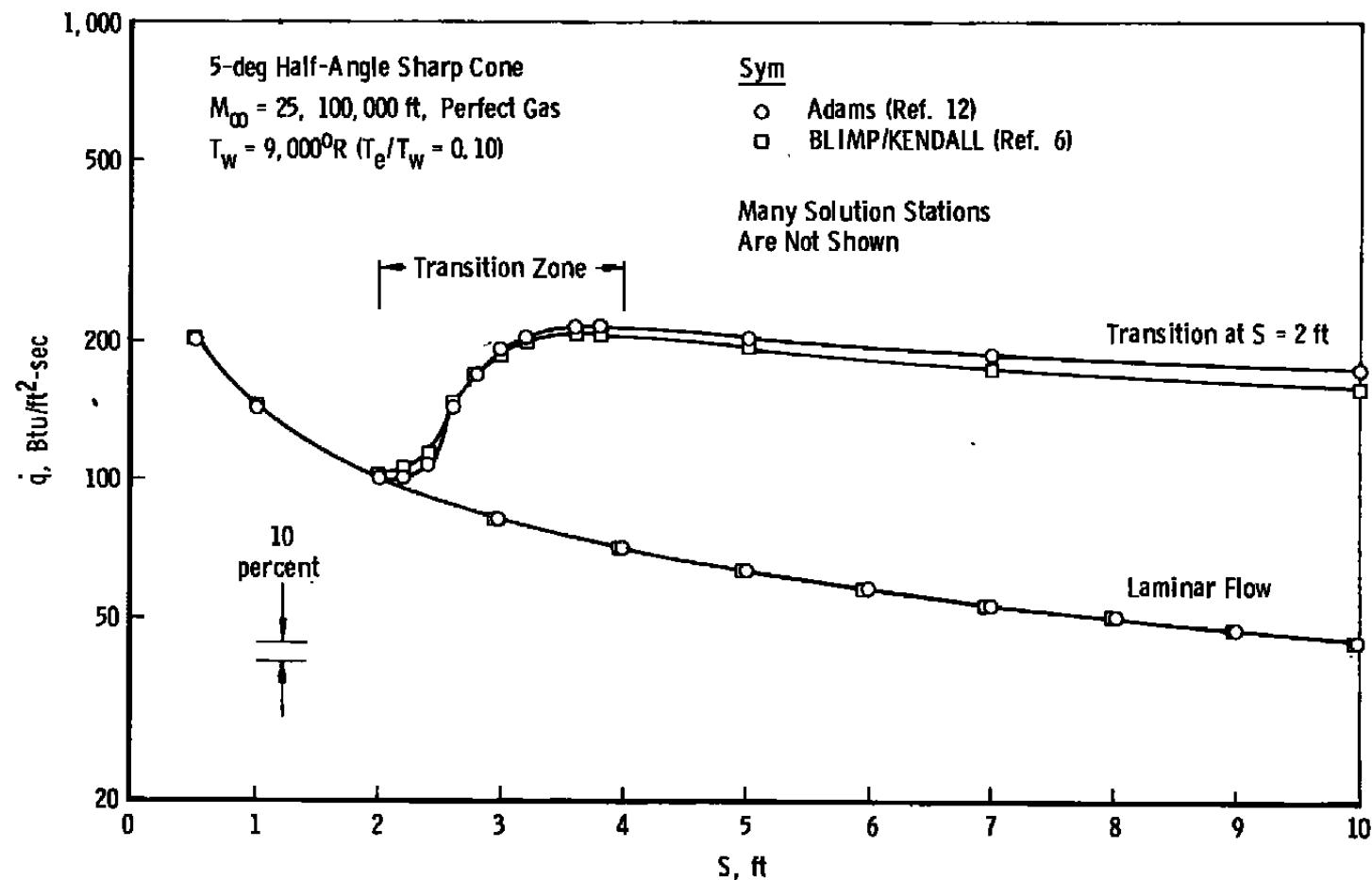
c. T_w = 9,000°R
Figure 1. Concluded.
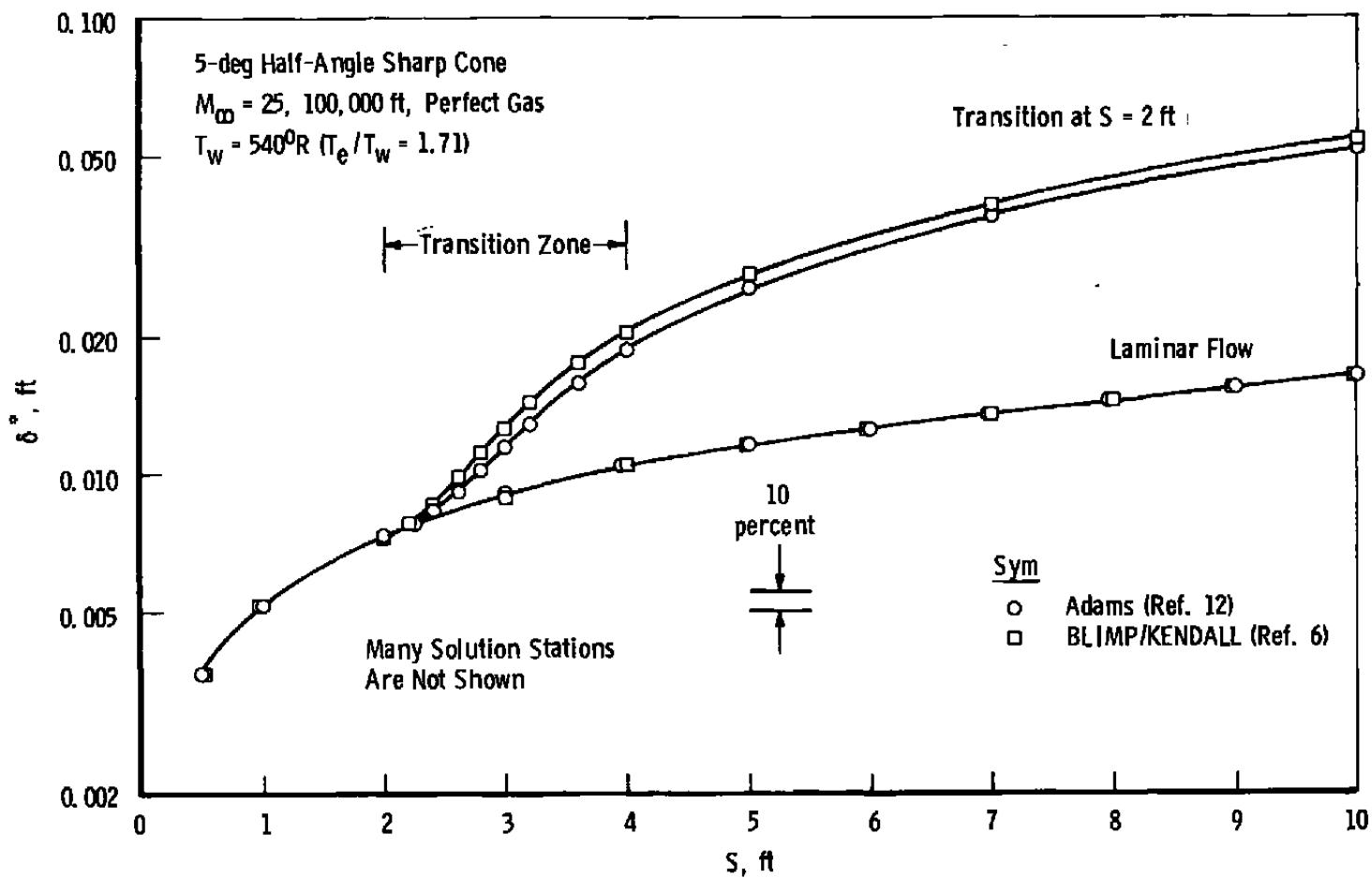
Figure 2. Calculation of the boundary-layer displacement thickness on a
sharp cone at reentry conditions from two different
boundary-layer solution methods.
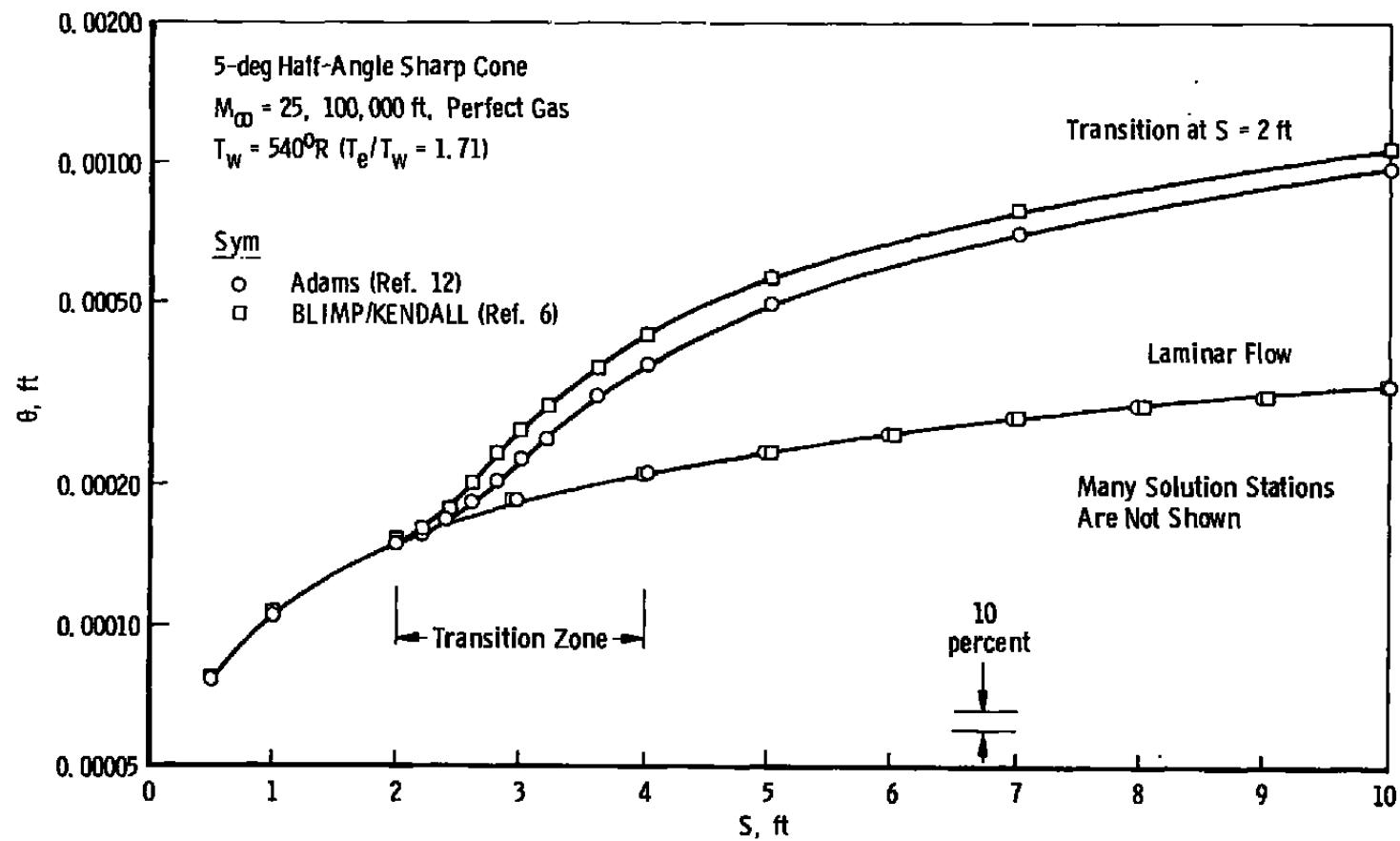
Figure 3. Calculation of the boundary-layer momentum thickness on a sharp cone at reentry conditions from two different boundary-layer solution methods.
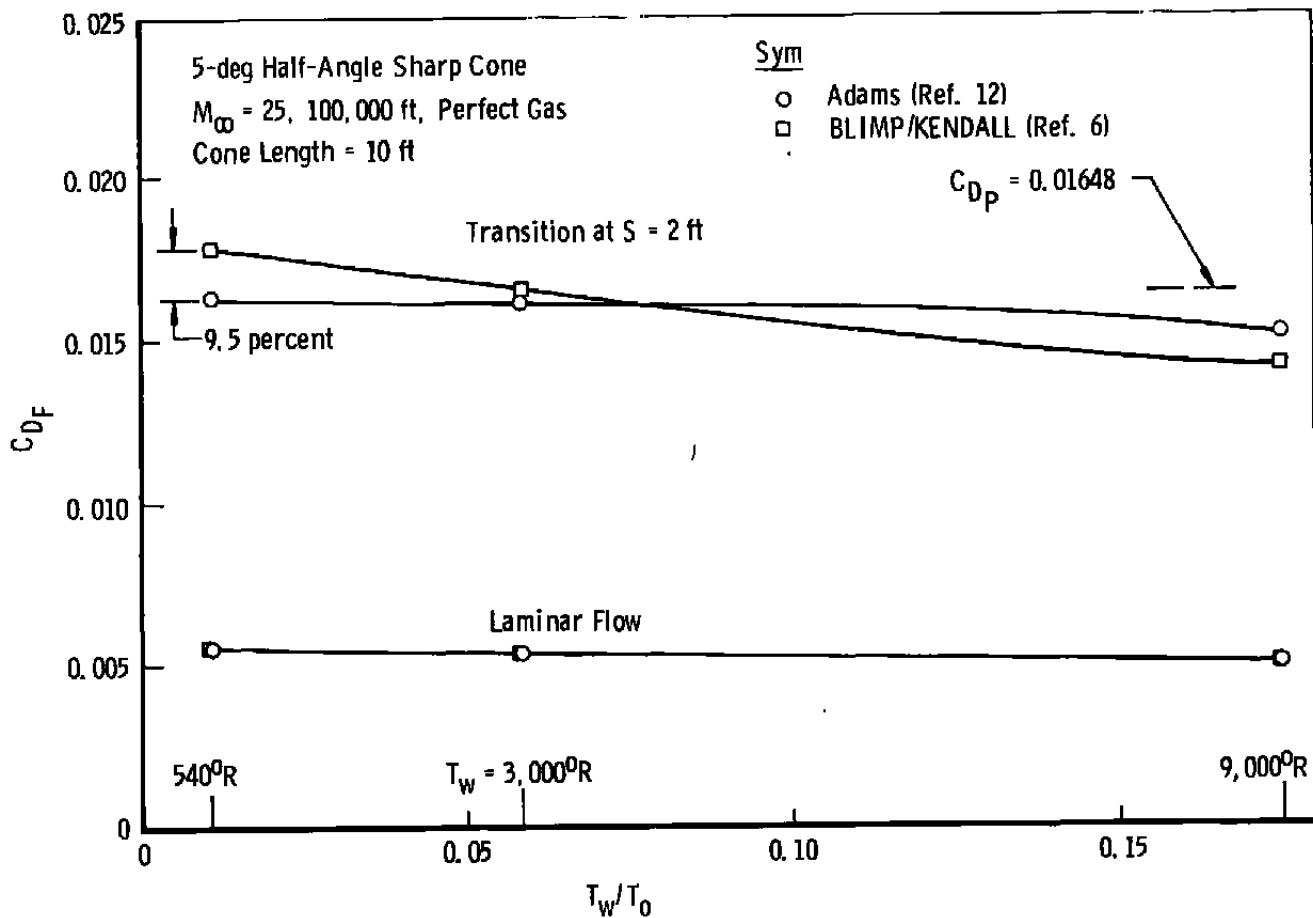
Figure 4. Variation of the skin-friction drag coefficient with wall temperature for a sharp cone at reentry conditions.
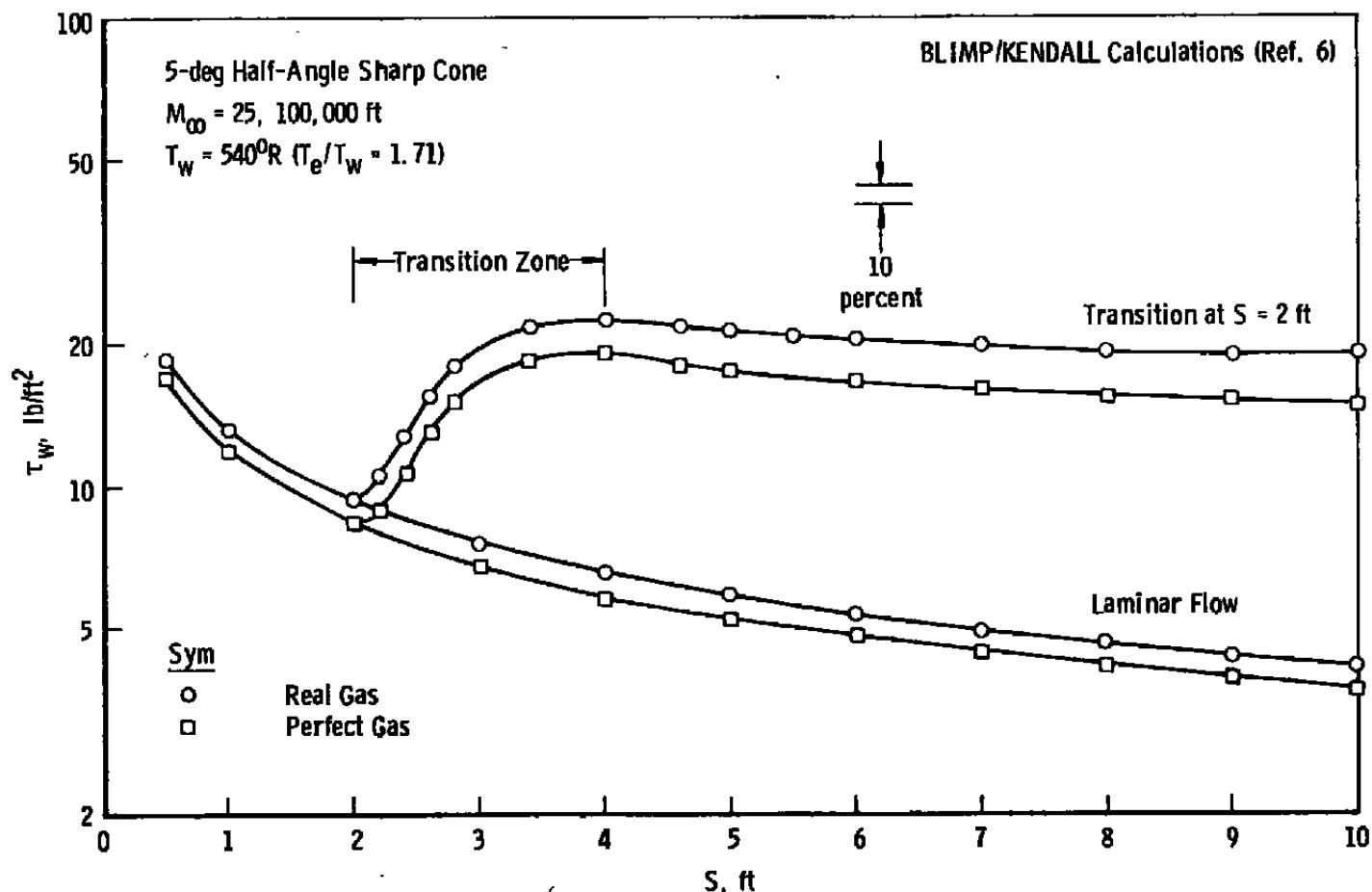
a. T_w = 540°R

Figure 5.   Real gas effects on the calculation of wall shear stress
for a sharp cone at reentry conditions.
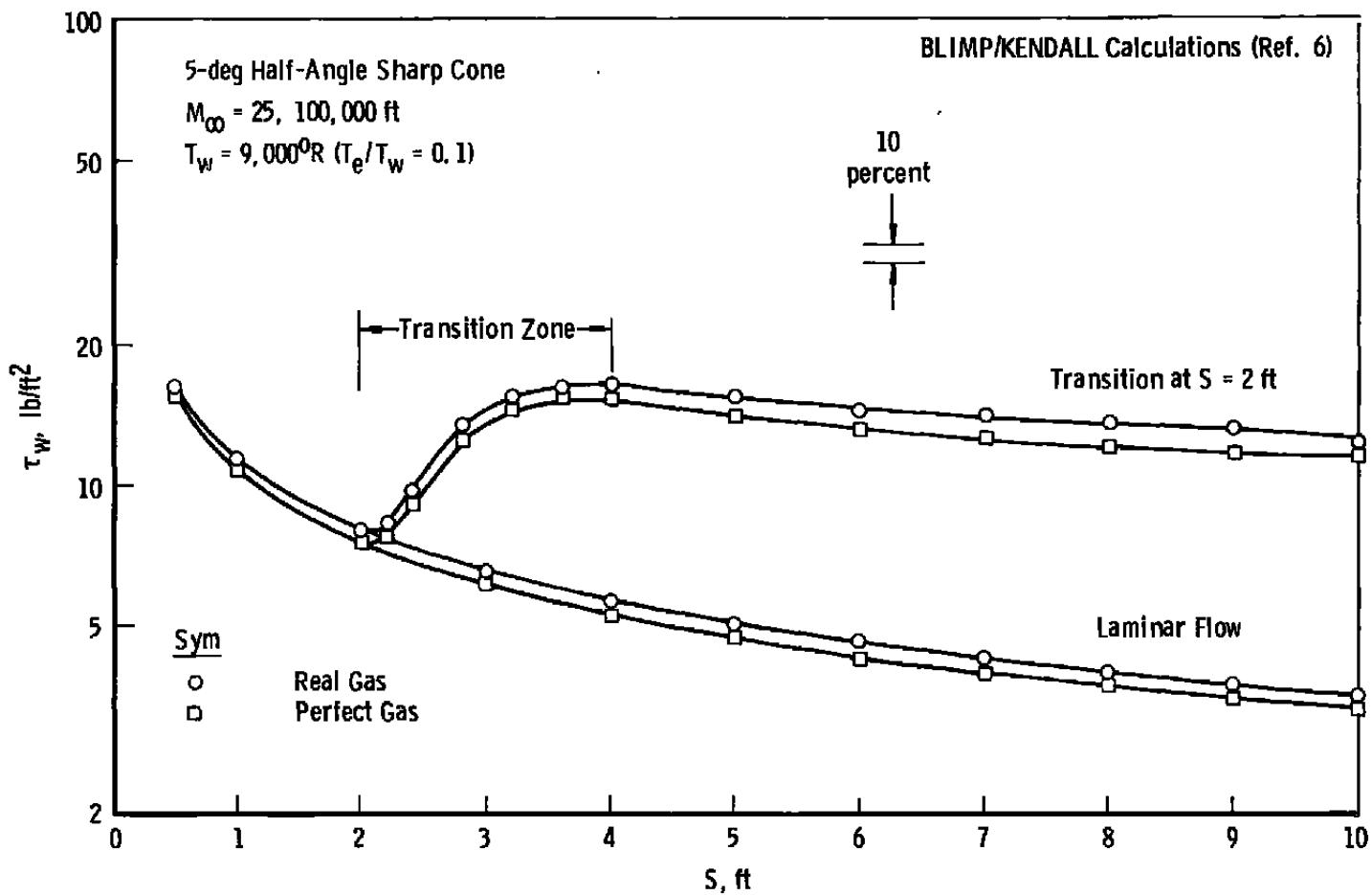
b. $T_w = 9,000°R$

Figure 5. Concluded.
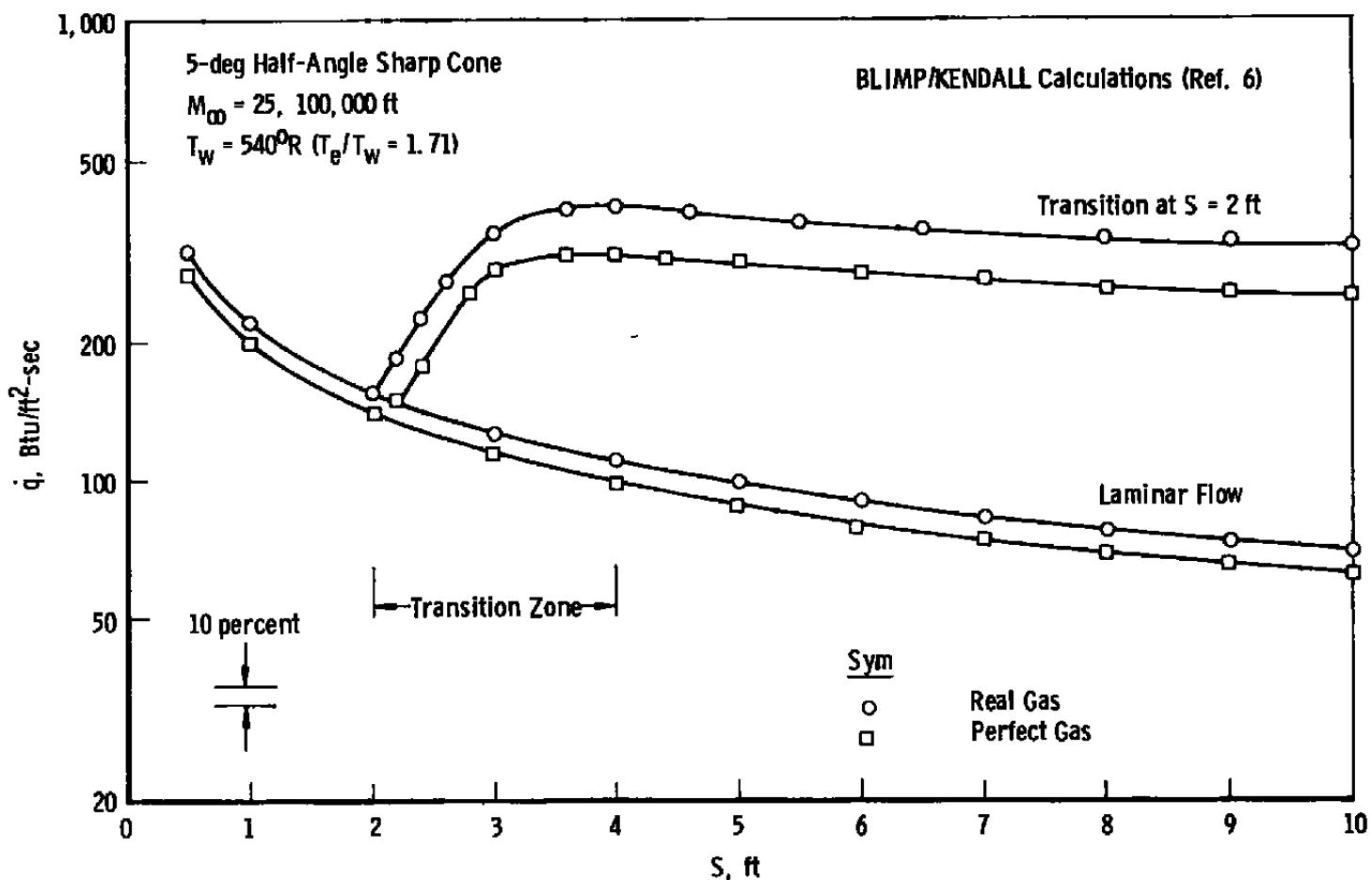
a. $T_w = 540°R$

Figure 6. Real gas effects on the calculation of wall heat-transfer
rates for a sharp cone at reentry conditions.
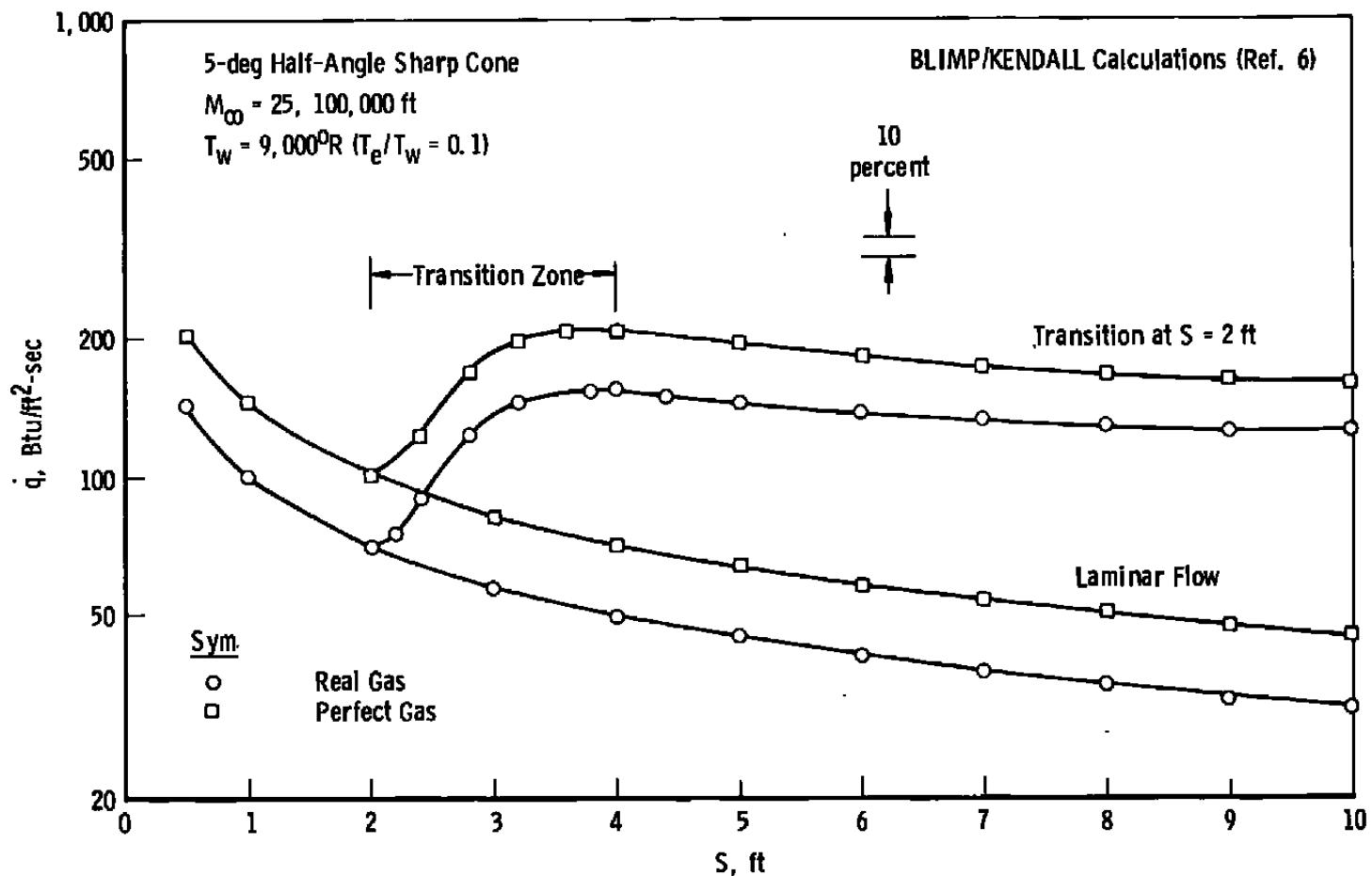
b. $T_w = 9,000°R$

Figure 6. Concluded.
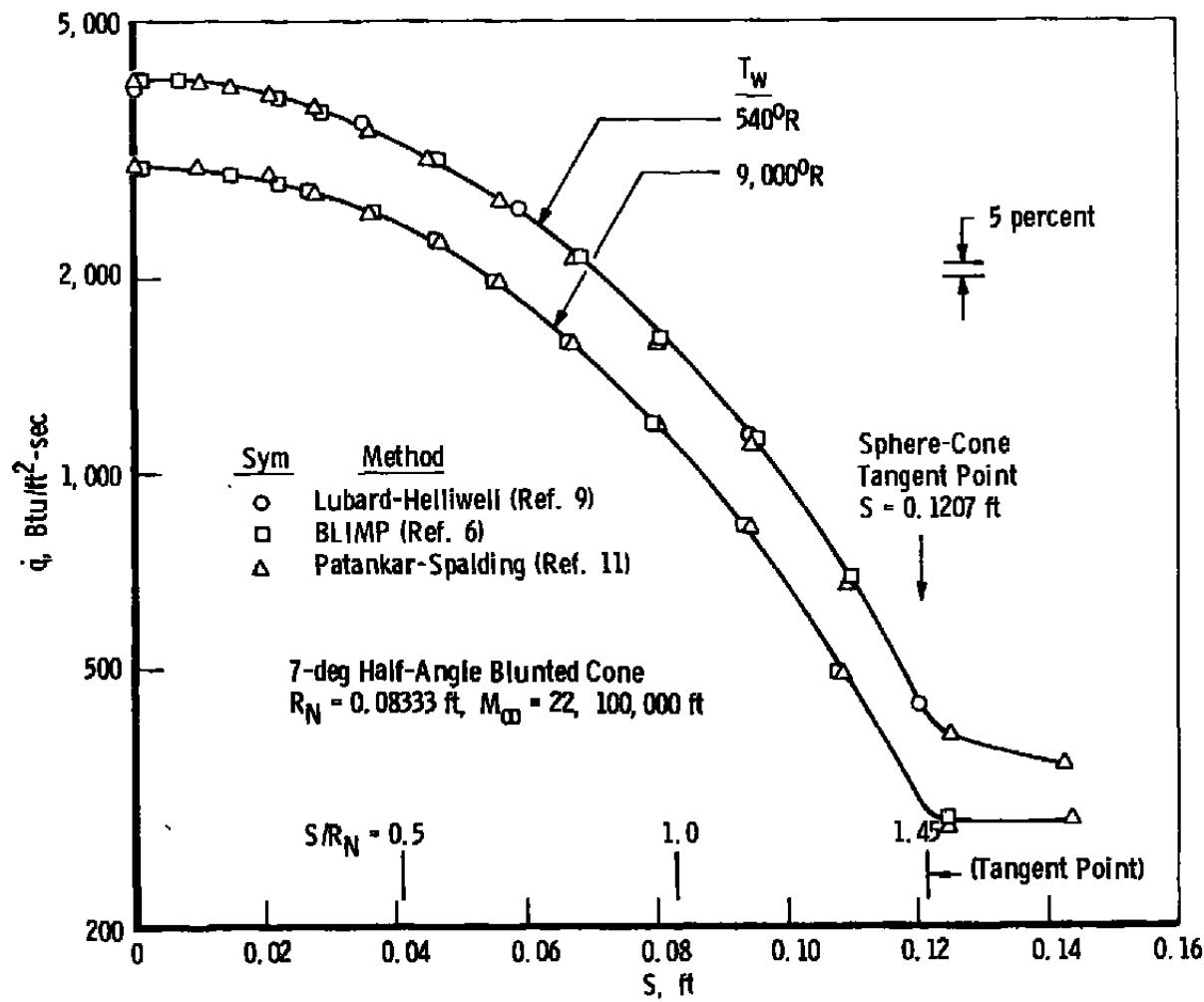
Figure 7. Perfect gas heat-transfer rate comparisons in the spherical
region of a reentry body.
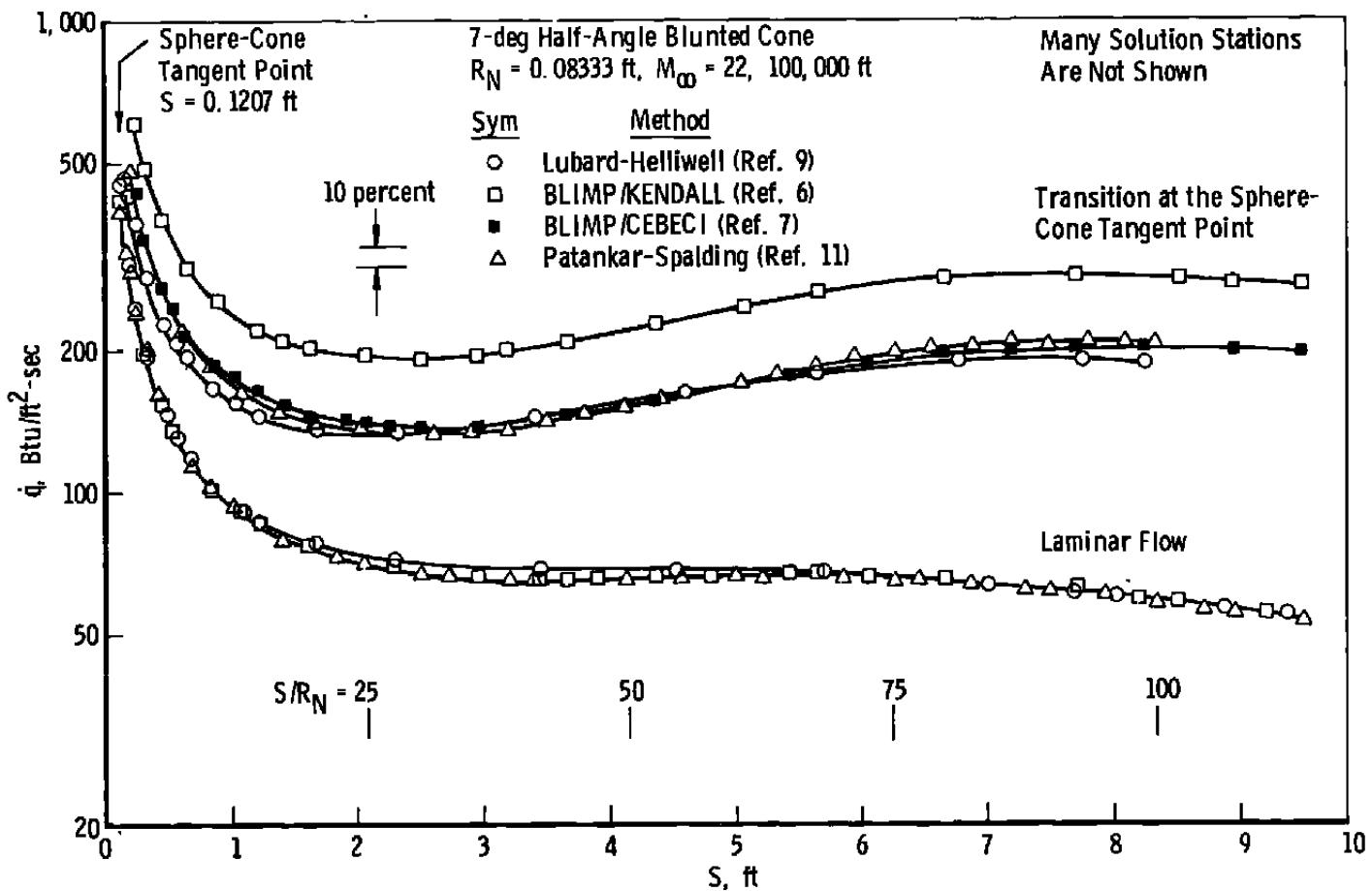
a. $T_w = 540°R$

Figure 8. Perfect gas heat-transfer rate comparisons on the afterbody
of a reentry body.
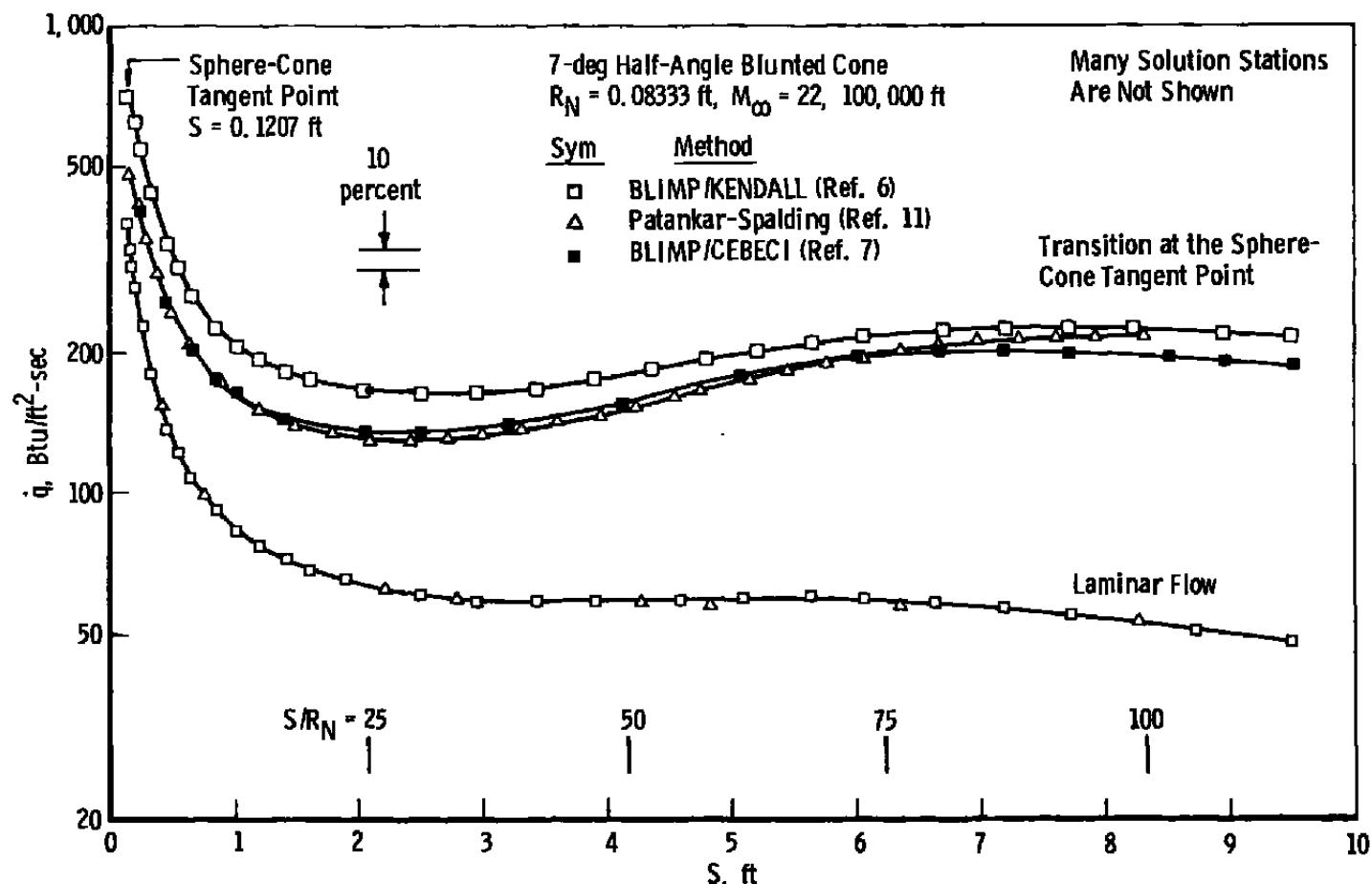
b. $T_w = 3,000°R$

Figure 8. Continued.

c. $T_w = 9,000°R$
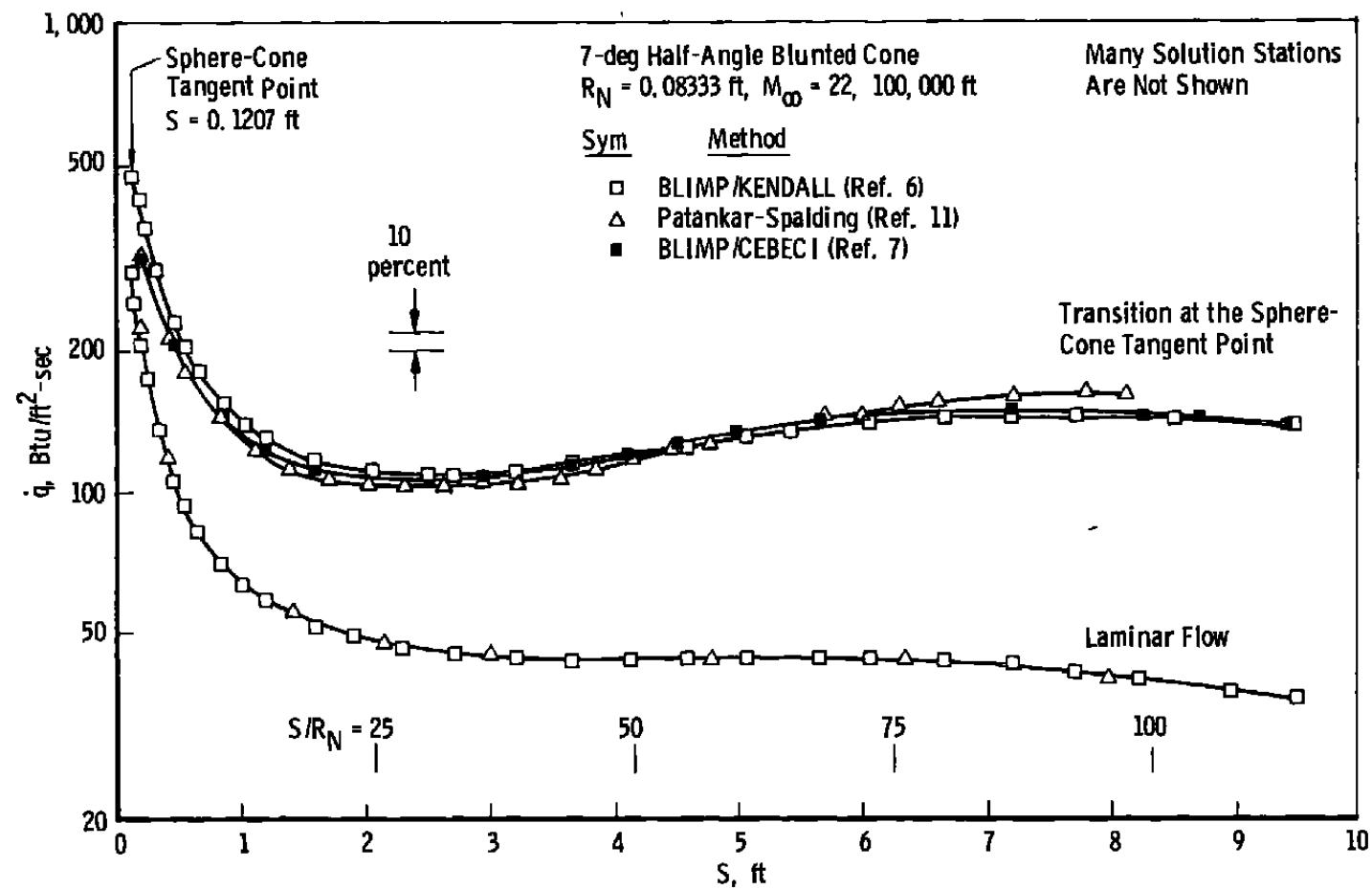
Figure 8. Concluded.
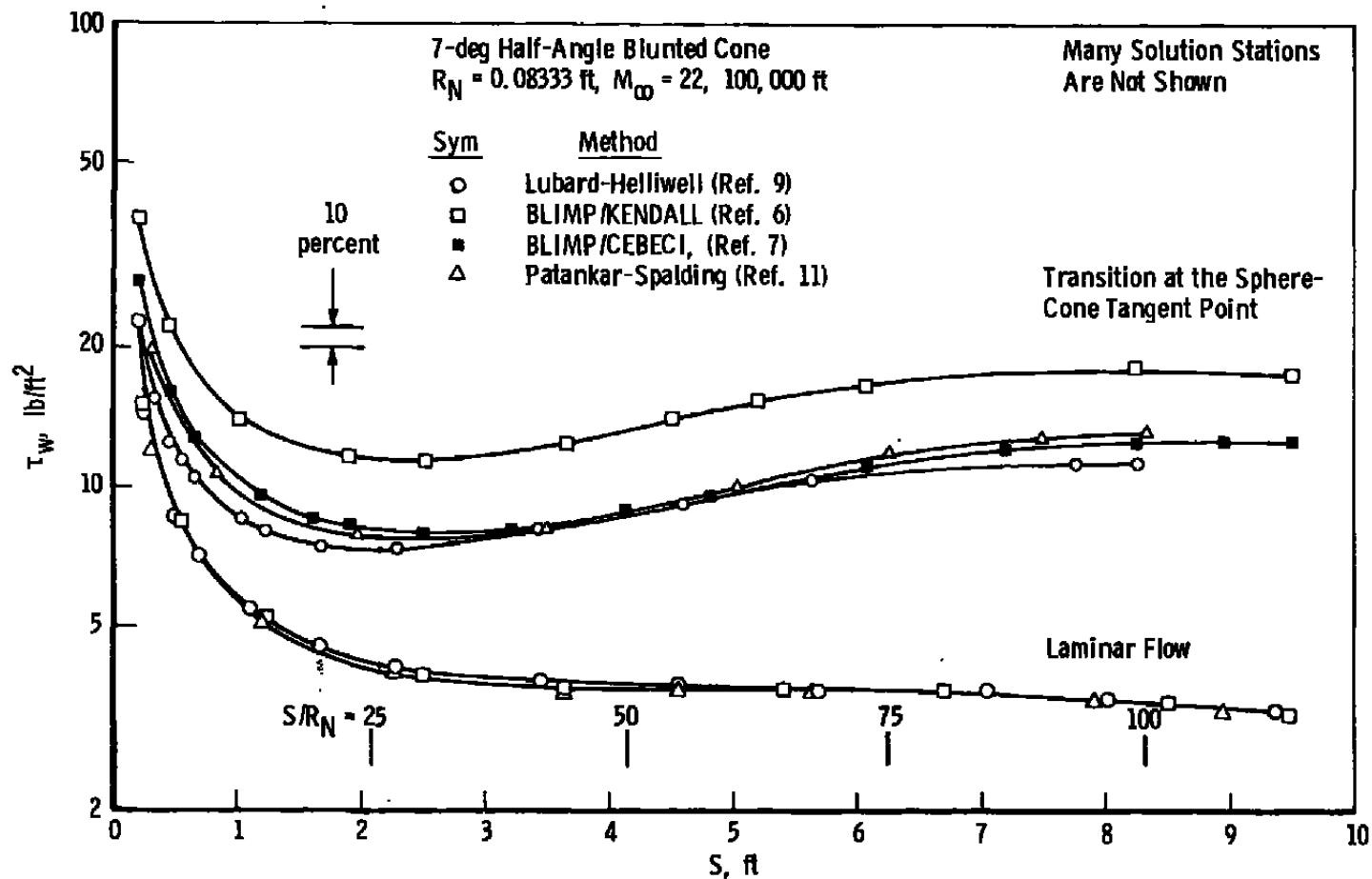
Figure 9. Perfect gas wall shear stress comparisons on the afterbody of a reentry body at $T_w = 540°R$.
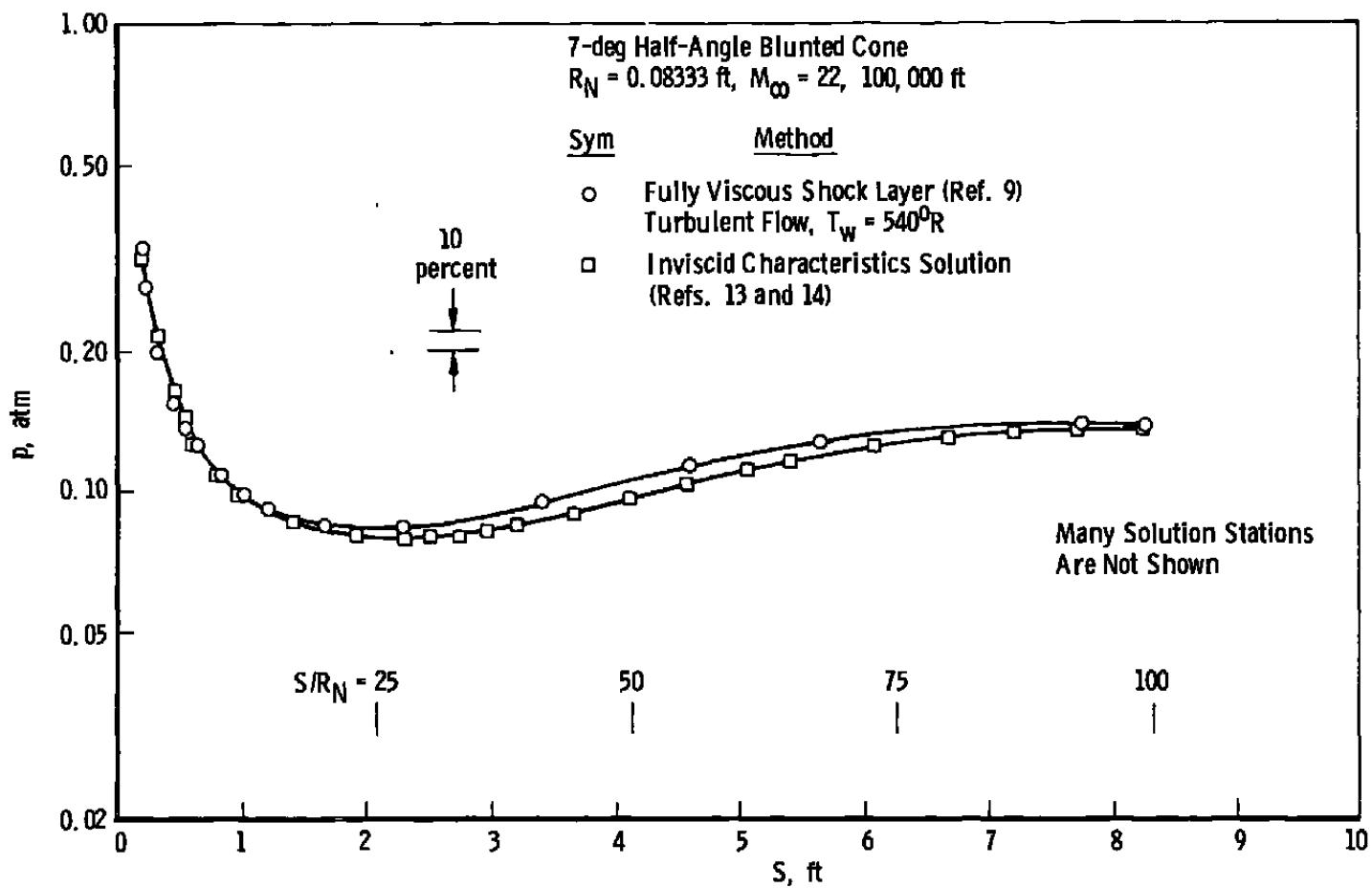
Figure 10. Boundary-layer displacement effects on the pressure distribution
for the turbulent boundary layer, T_w = 540°R, perfect gas.
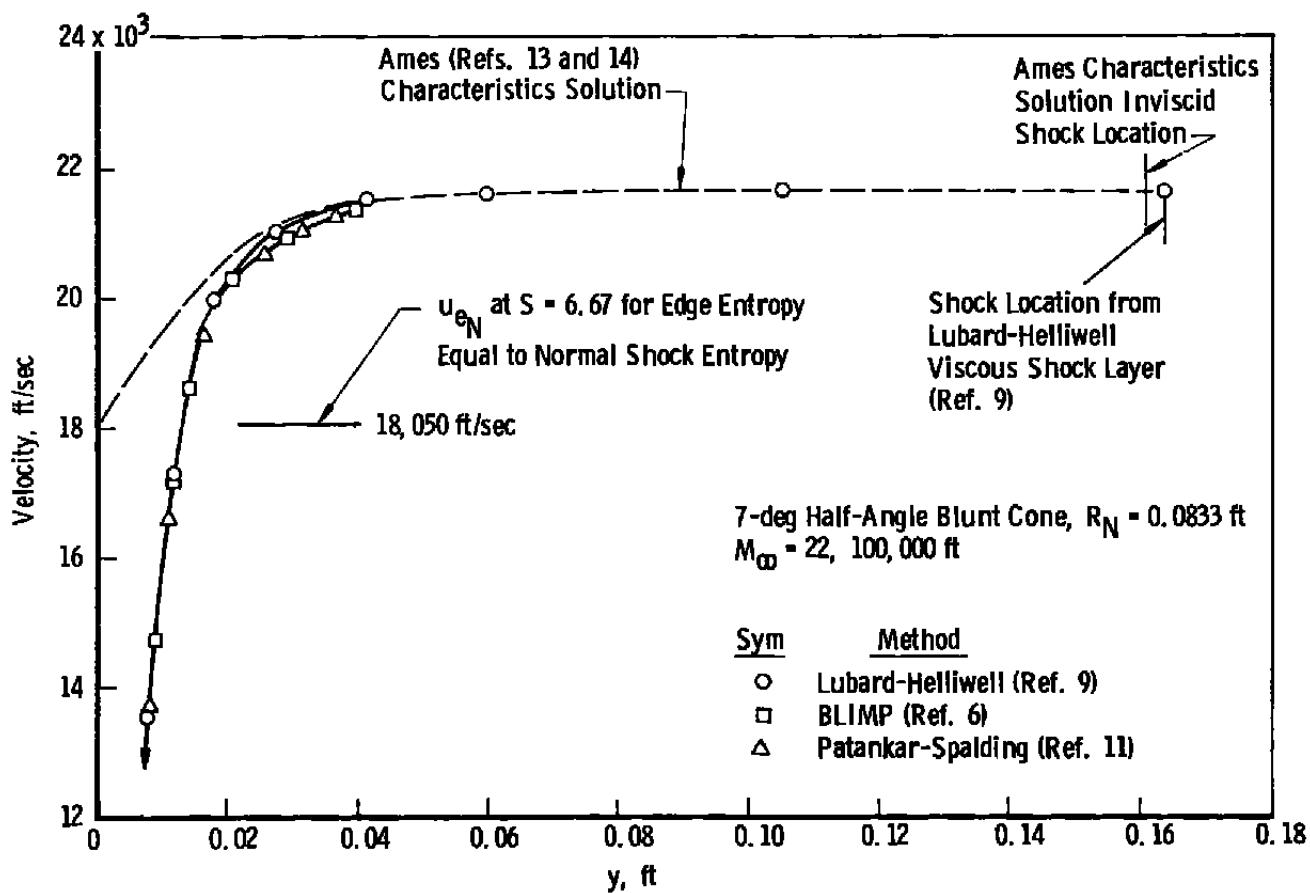
Figure 11. Velocity distributions through the shock layer at S = 6.67 ft
for laminar flow. T_w = 540°R, perfect gas.
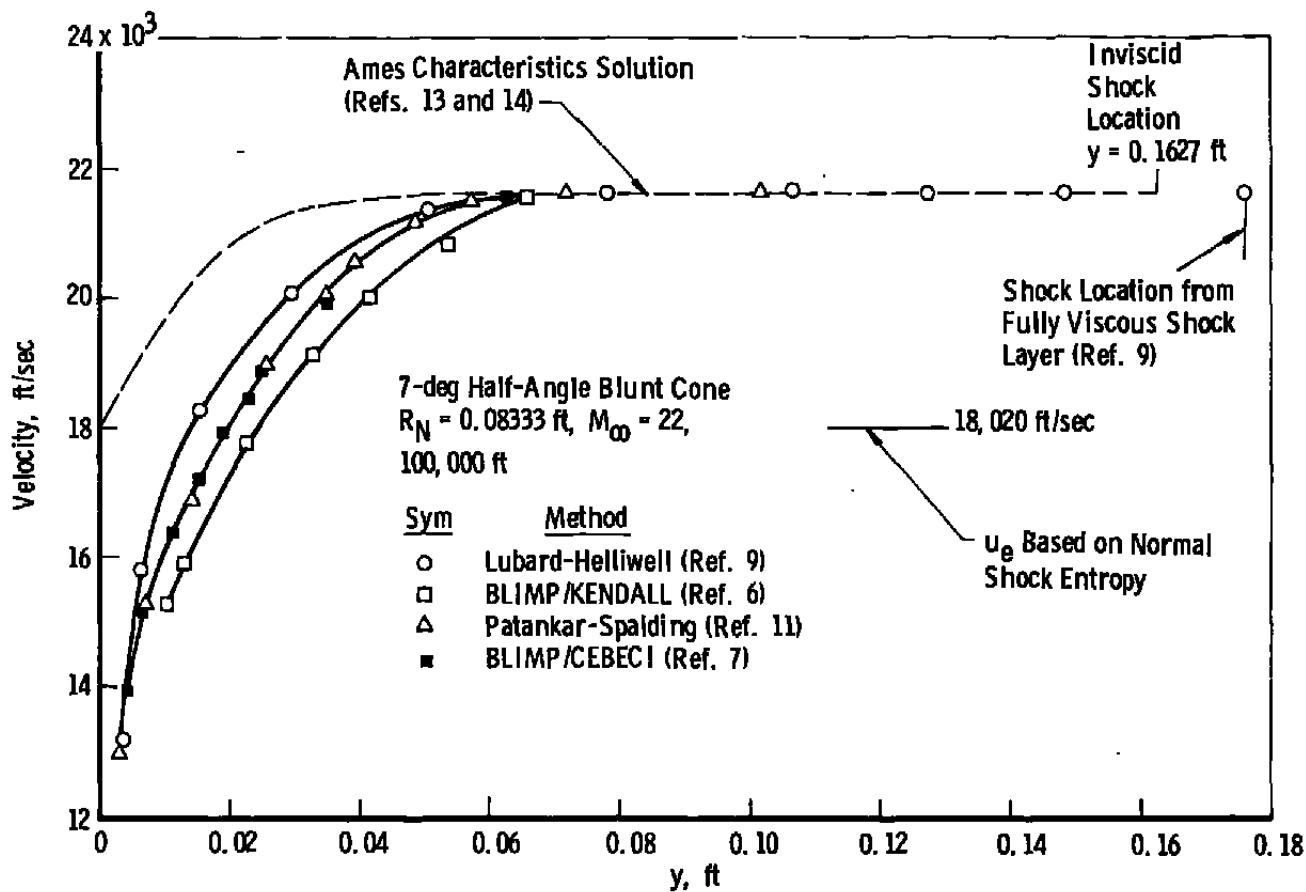
Figure 12. Velocity distributions through the shock layer at S = 7.18 ft
for turbulent flow, T_w = 540°R, perfect gas.
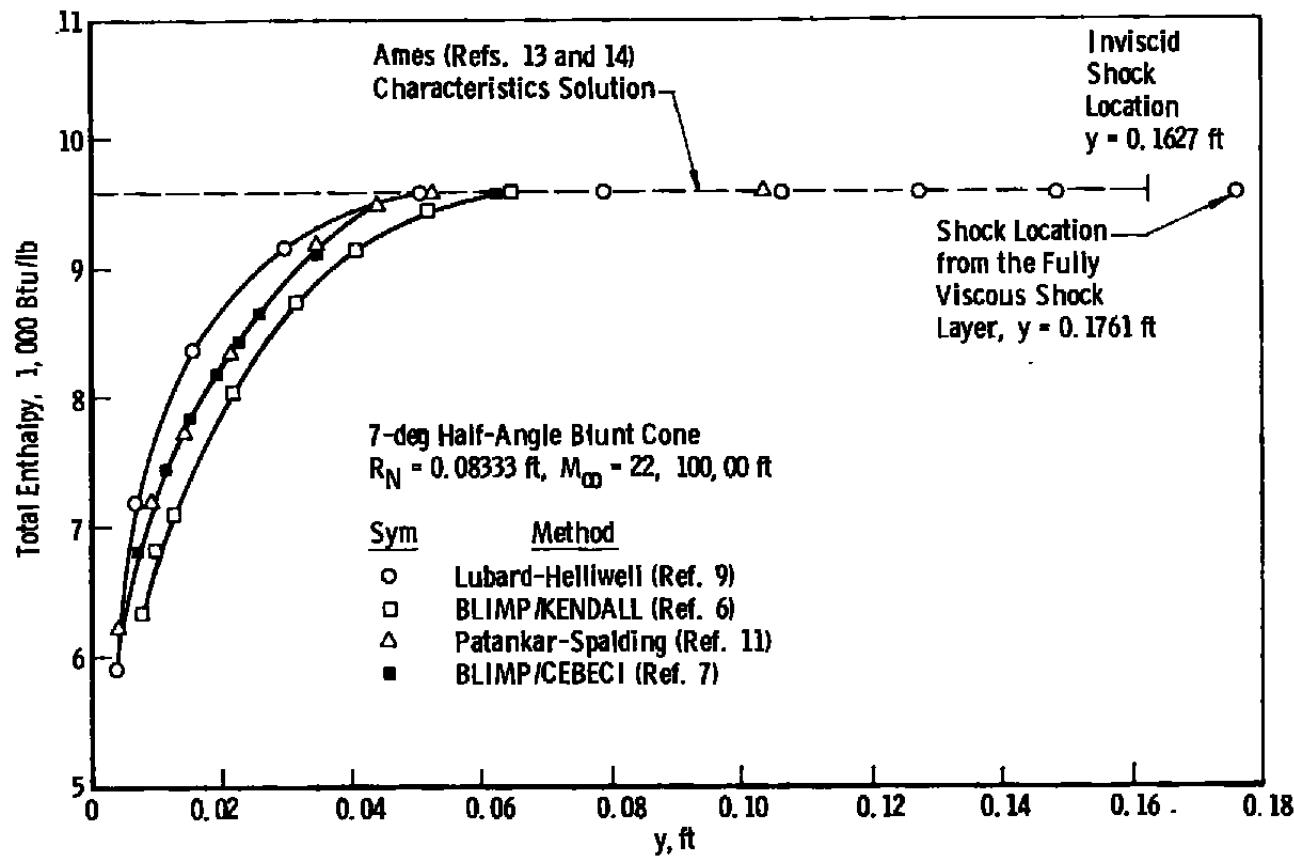
Figure 13. Total enthalpy profiles through the shock layer at S = 7.18 ft for turbulent flow, T_w = 540°R, perfect gas.
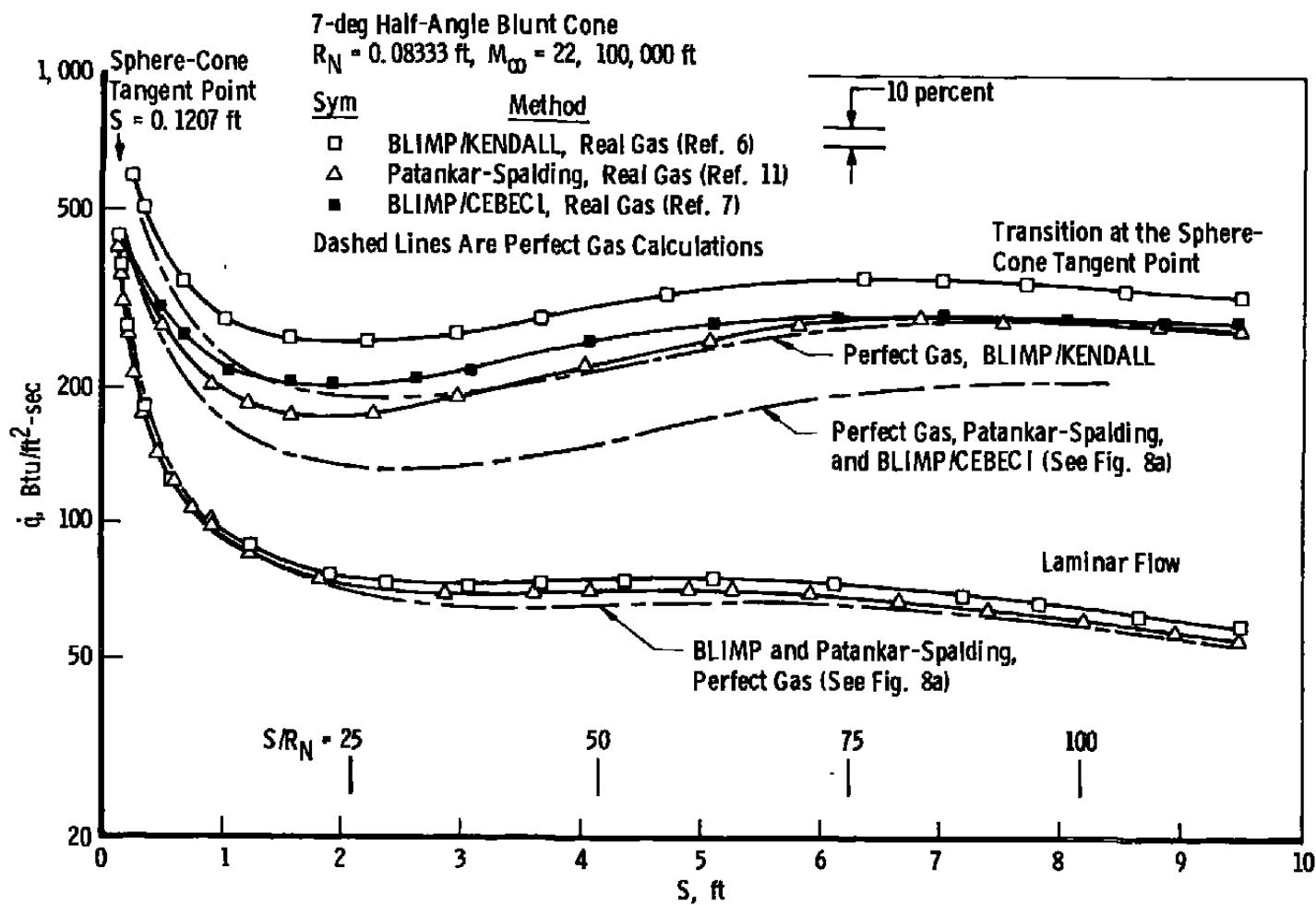
a. With different theories and turbulence models

Figure 14. Real gas effects on the afterbody heat-transfer rates, $T_w = 540°R$.
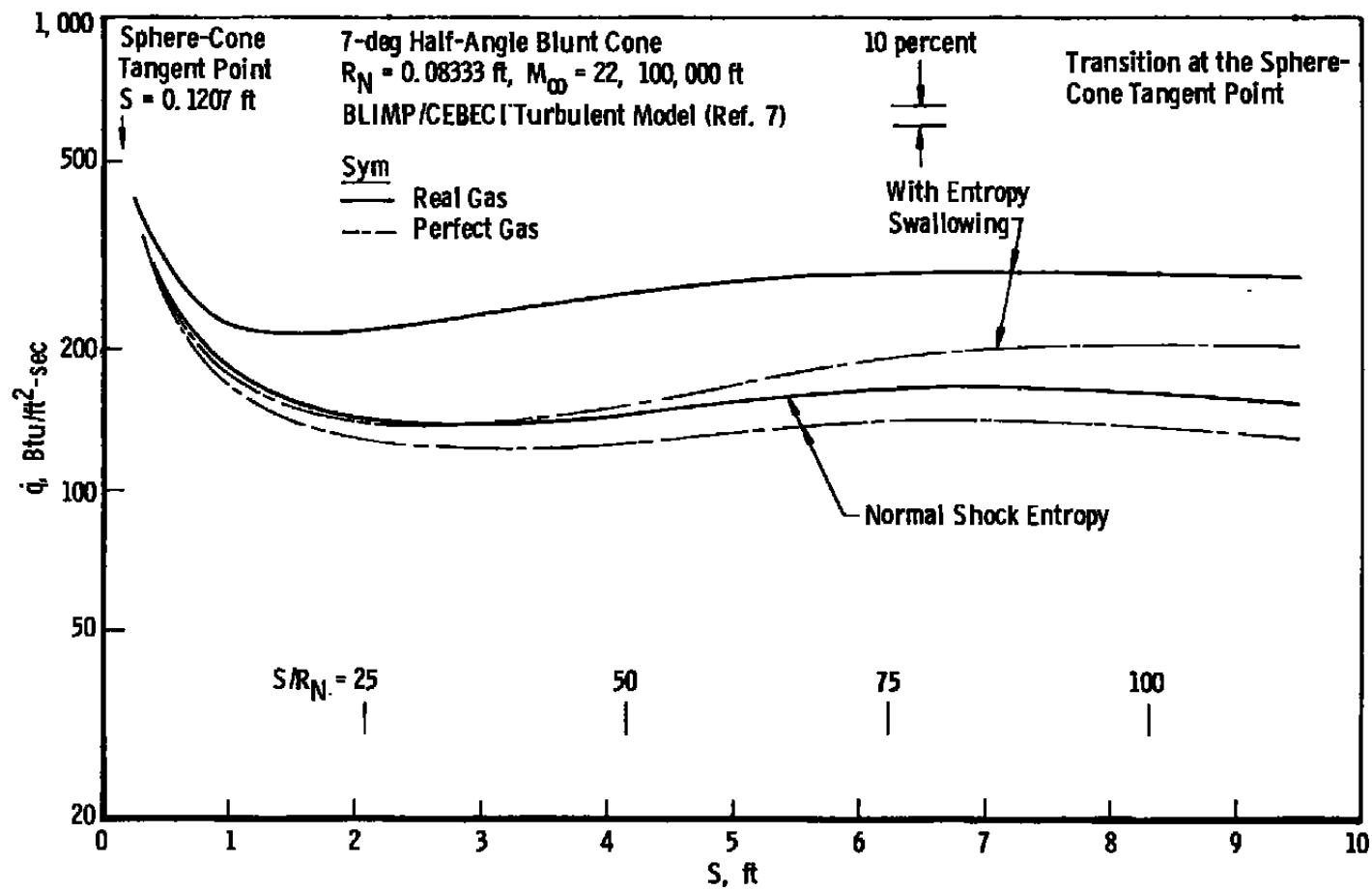
b. With and without entropy swallowing for turbulent
   flow (BLIMP/CEBECI)

Figure 14. Continued.
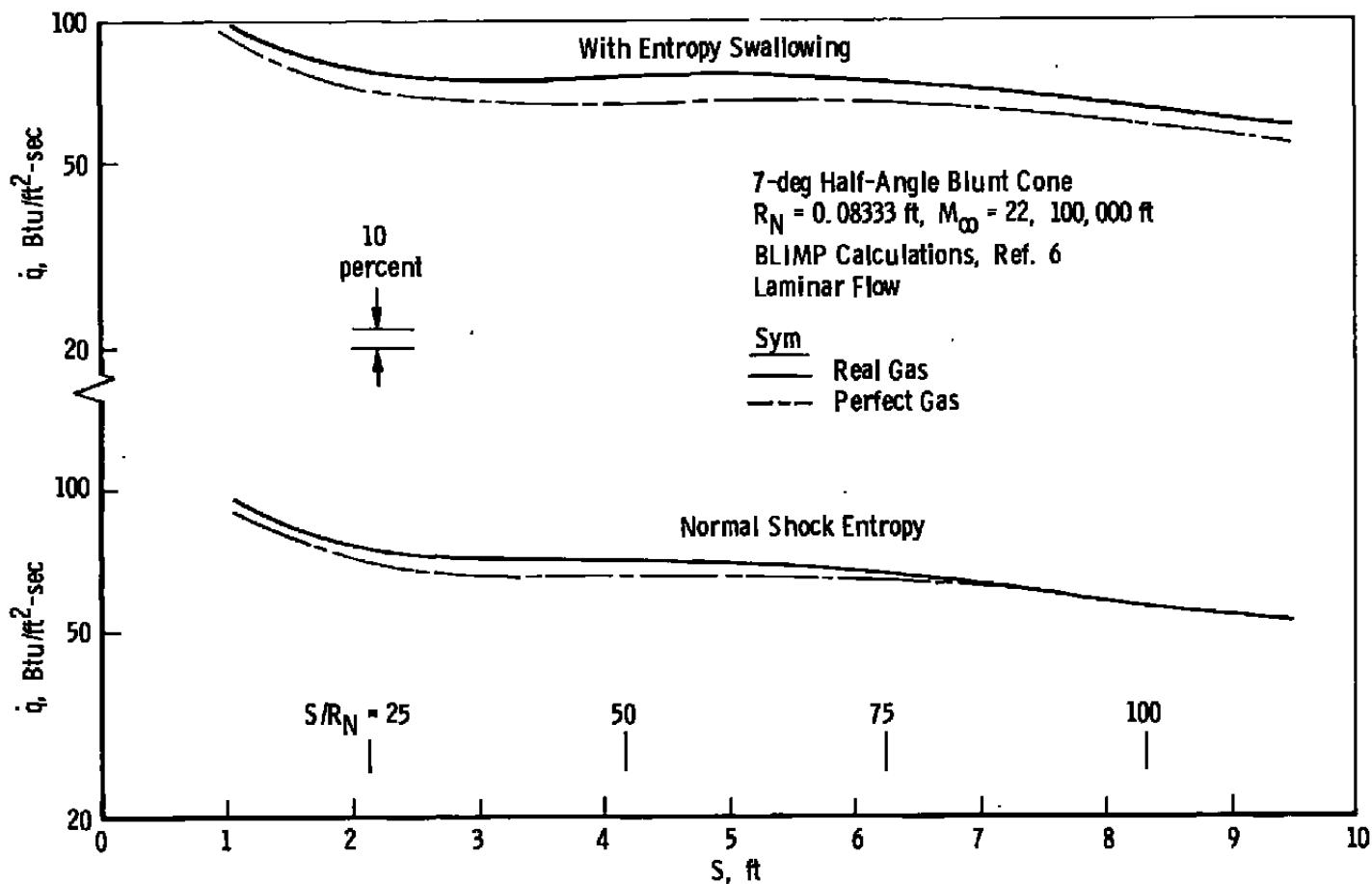
c. With and without entropy swallowing for laminar flow (BLIMP)
Figure 14. Concluded.
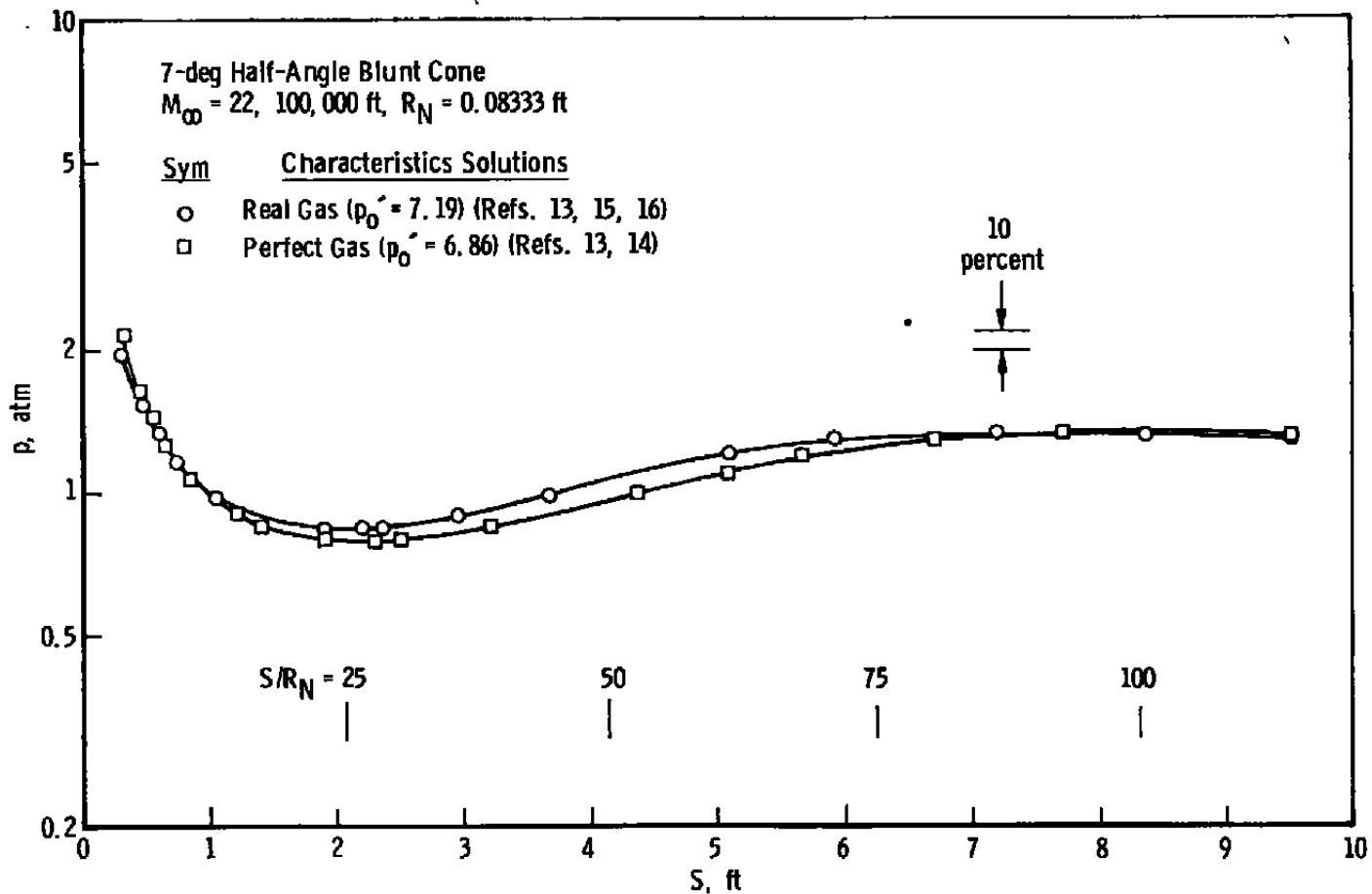
Figure 15. Real gas effects on the afterbody pressure distribution.

Reference Values for ΔS

Entropy behind the Normal Shock, Real Gas = 2.97 Btu/lb-$^{\circ}$R
Entropy behind the Normal Shock, Perfect Gas = 2.66 Btu/lb-$^{\circ}$R
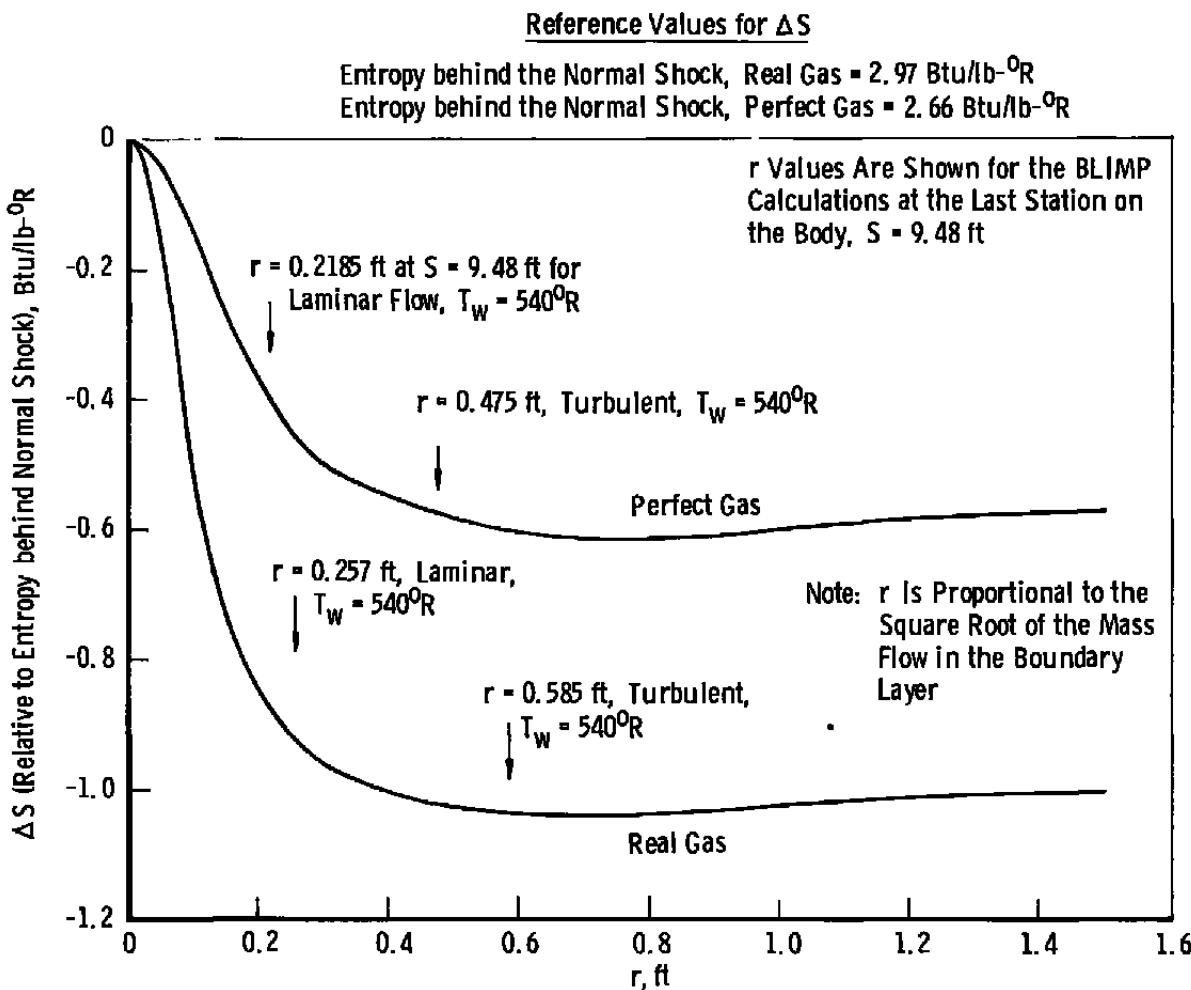
Figure 16. Real gas effects on the entropy rise across the shock,
R_N = 0.08333 ft, M_∞ = 22, 100,000-ft altitude.

1.00

0.50

5-deg Half-Angle Cone
Time = 456.4 sec, 77,000 ft, α = 0.35 deg,
M_∞ = 19.92, Re_∞/ft = 6.47 x 10^6, T_w = 1,000°R

Sharp Cone Inviscid
Solution of Jones (Ref. 28)

Windward

0.20   Leeward

p, atm

0.10

10 percent

Sym   Experimental Data (Ref. 24)
O   0-deg Ray (Leeward)
◊   90-deg Ray or 270-deg Ray
□   180-deg Ray (Windward)

0.05

0.02
0   3   4   5   6   7   8   9   10   11   12

S, ft
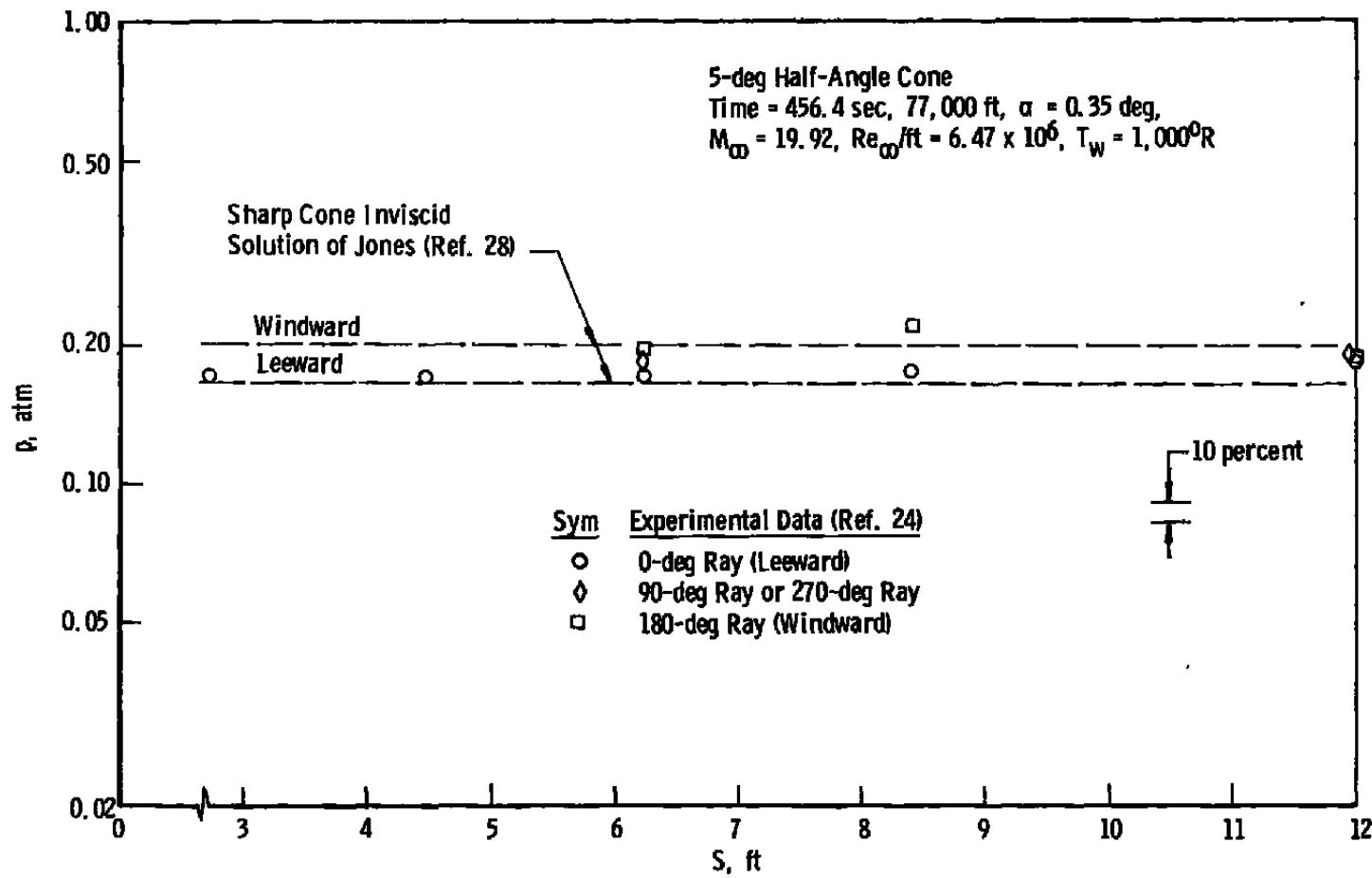
Figure 17. Pressure measurements on the Reentry F spacecraft
compared with inviscid sharp cone theory.
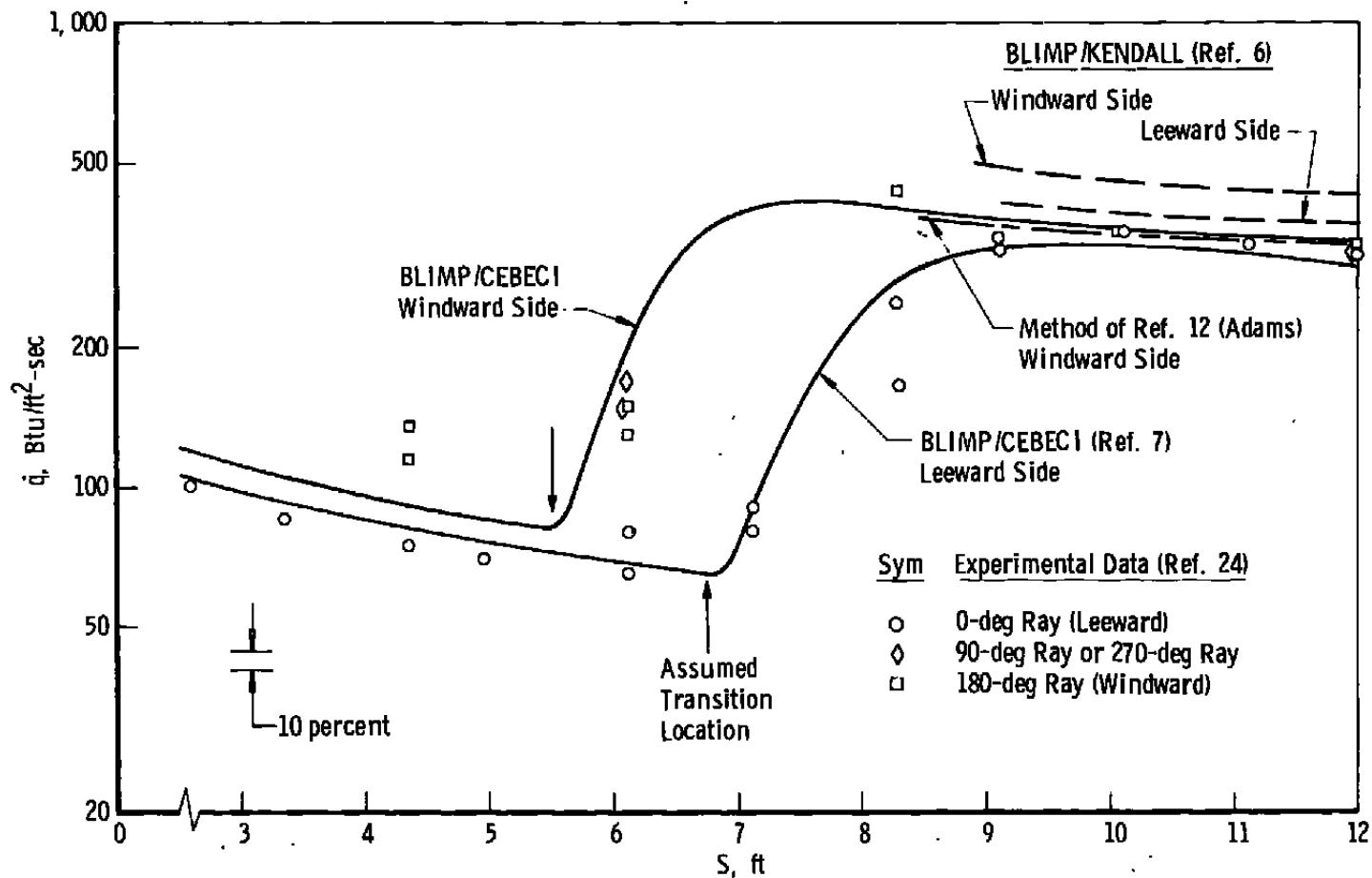
Figure 18. Comparison of theory and experiment for the heat-transfer
rate distribution on a reentry vehicle (Reentry F).

APPENDIX A

CHOICE OF A SIMPLE AIR CHEMISTRY MODEL FOR NONABLATING BOUNDARY-LAYER PROBLEMS

The input options for BLIMP allow a flexible choice of chemistry models to represent the boundary-layer gas. For the simple, nonablating, chemical-equilibrium case under consideration here, the input quantities which are used to specify the chemistry model are: (1) the mass fractions and atomic weights of the various elements present, (2) certain data for each of the candidate chemical species (molecular, atomic, ionic, or electron species) including heats of formation, and curve-fit constants which define the variation of specific heat (C_p), enthalpy and entropy over a temperature range (at a pressure of one atmosphere), and (3) diffusion factors for each candidate species, which are used ultimately to calculate the transport properties of the multicomponent boundary layer gas. If a state of thermodynamic and chemical equilibrium exists the relative amounts of the chemical species present can be determined (from the candidate species) when two independent thermodynamic variables are specified (for boundary-layer solutions, these are known from the inviscid pressure distribution, and either a wall condition (T_w, for example) or a boundary-layer edge condition, or the boundary-layer solution itself).

The BLIMP user has control over which candidate species are to be considered for a particular problem. For example, if it is known that the reaction rate for the formation of a particular species is very slow, the BLIMP user may delete the data for this species from the input deck, and it will not be considered in the problem. Similarly, the equilibrium thermodynamic conditions might be in a range such that the amount of a particular species present is minimal, and again it would be desirable to delete this species from consideration to speed up the BLIMP calculations (e.g., ionic species need not be included for a low temperature wind tunnel problem). It was the objective here to determine a simple chemistry model for air (minimum number of candidate species) to be used for nonablating high altitude problems which would still give accurate results for the thermodynamic and transport properties. The ionic species could be deleted from this basic model for low temperature wind tunnel problems. The gas was considered to be in chemical equilibrium.

The starting point for the chemistry model determination was the work reported by Deblaye and Bartlett in Ref. 29. Deblaye and Bartlett determined an appropriate chemistry model for an ablating C-H-O-N-e$^-$ elemental system, and included in their report a comprehensive model for air which was evaluated by comparisons with data from many other sources. The reader is referred to this report for a discussion of the thermodynamic and transport property modeling used in the BLIMP program. The Deblaye and Bartlett air

model is summarized in the form of BLIMP input data in Table 3, p. 23, and Table VI on p. 56 of Ref. 29. The data in Table 3 also include the various C-H species and these were eliminated to get the air model.

Starting with these data several computer runs were made at AEDC using the ACE Code (Aerotherm Chemical Equilbrium Code, Ref. 30) to determine which species were present in significant quantities over a pressure range from 0.0001 to 1,000 atm and a temperature range from 20 to 10,000°K. Unimportant species were eliminated, and then the thermodynamic properties were compared with the data of Brahinsky (Ref. 31, which is based largely on the data of Hilsenrath, Ref. 32) and the transport properties with the calculations of Yos (Ref. 33). The elemental mass fractions used for the BLIMP chemistry model are the same as Hilsenrath (Ref. 32) except that the very small amounts of CO_2 and Ne were left out of the BLIMP model.

The resulting chemistry model is given in BLIMP-input form in Table A-1. The model is a 10-species model including these species: O_2, N_2, O, N, NO, A, e-, N^+, NO^+ and O^+. The ionic species were included to better model the transport properties at low pressure (p = 0.0001 atm) and high temperature (T > 8,000°K). (A 10-percent discrepancy in frozen thermal conductivity was obtained at p = 0.0001 atm and T = 8,000°K without the electrons, and 20 percent at T = 9,000°K). For nonablating reentry (T < 8,000°K) problems, these ionic species could be eliminated. Also, argon was incorporated to facilitate comparisons with the Hilsenrath data (which also included argon) and may be eliminated. Thus for many wind tunnel and high-altitude nonablating reentry problems, a chemistry model composed of 5 species is proposed, namely: O_2, N_2, O, N and NO.

Comparison of the 10-species model results for density and enthalpy with results tabulated by Brahinsky (Ref. 31) is given in Figs. A-1 and A-2. Note that very good agreement is obtained up through a pressure of 100 atm. The high-pressure effects incorporated in the Brahinsky data begin to show up on the density results at pressures just above 100 atm (not shown in graph) and are significant at p = 1,000 atm at the lower temperatures. Further comparisons with other data sources are presented in Tables A-2 (enthalpy) and A-3 (specific heat at constant pressure) at the higher temperatures. Although they are not plotted here, the other pertinent thermodynamic variables were also compared versus the data of Brahinsky or Hilsenrath (mole fractions, entropy, molecular weight).

The thermodynamic curve fits were extended to lower temperatures during this study by adding a third temperature range to the BLIMP code, producing C_p curve fits accurate down to 20°K. The data provided in Table A-1 include this extended temperature range.

Graphs of the transport property calculations at a pressure of one atm are presented in Figs. A-3 and A-4. The standards of comparison given here are the data of Yos (Ref. 33) for high temperatures and the Sutherland equation presented in Ref. 23 at low temperatures (with $Pr = 0.71$ and $C_p = 0.23989$ Btu/lb). A linear extrapolation of the Sutherland viscosity equation is used at temperatures below $100°K$. The data of Hansen, Ref. 36, are also shown at low temperatures.

By referring to Figs. A-3 and A-4b, it may be seen that the BLIMP chemistry model (principally the diffusion factors) should not be used for temperatures less than $200°K$ because of poor agreement of the thermal conductivity and viscosity data with the Sutherland equation. The Sutherland equation and the Hansen data are in good agreement at the low temperatures.

The BLIMP calculations compare well with the Yos calculations up to temperatures of 4,000 to $5,000°K$ at a pressure of 1 atm. There is very little effect of pressure on either viscosity or thermal conductivity given by Yos up to the highest pressure tabulated (30 atm) at temperatures of $5,000°K$ or below. BLIMP also gives a small effect of pressure at these conditions.

In summary, a simple 10-species chemistry model for air is given here which represents very well the air thermodynamic properties for the pressure range from 0.0001 to 100 atm and the temperature range from 20 to $10,000°K$. Transport properties are represented reasonably well in the temperature range from $200°K$ to $4,000°K$. This latter temperature range is sufficient for most nonablating reentry conditions. For certain wind tunnel calculations with sharp cone models, temperatures may be below $200°K$, and the homogeneous option of BLIMP should be used together with the Sutherland viscosity equation with $C_p = 0.23989$ Btu/lb and $Pr = 0.71$. The real gas calculations presented in this report were made using the 10-species chemistry model. For most nonablating reentry calculations and wind tunnel calculations, comparable accuracy would be obtained using a still simpler 5-species chemistry model consisting of O_2, N_2, O, N and NO.

Table A-1. BLIMP Code Inputs for the Simple Chemistry Model

```
 7 NITROGEN      14.008    -.7555 ⌐
 8 OXYGEN        16.000    -.2315 ├─ Elemental Mass Fractions
18 ARGON         39.948    -.013  ⌐
99 ELECTRON       0.00055
20
O2          0.955     O2      -1.003    N2       1.027    N2     -1.026 ⌐
O           0.706     O       -0.666    N        0.755    N      -0.749 │
NO          0.998     NO      -0.998    A        1.068    A      -1.068 ├─ Diffusion Factors
E-           .005     E-       -.008    NO+      1.059    NO+    -1.101 │
N+           .729     N+       -.779    O+        .778    O+      -.827 ⌐
   1 18   0   0   0   0   0   0   0   0   0   0   0DORRELL 11-05-74           A  ⌐
           134150+5 496470+1                      484500+2   0.   3000.1       A  │
           134150+5 496470+1                      484500+2   0.   3000.1       A  │
   2  8                                  GILMORE - JANAF                       O2 │
574000+0 234441+5 807265+1 503078-3-238837+6 679715+2 -500. 2500.1            O2 │
574000+0 234554+5 977777+1 110622-3-476367+7 679755+2 2500. 6000.1            O2 ├─ Curve-Fit Constants
574000+0 239896+5 671109+1 131479-2 891812+2 680258+2   20.  500.1            O2 │
   2  7                                  GILMORE - JANAF                       N2 │
-110000+0 222368+5 760394+1 501467-3-234708+6 637903+2 -500. 2500.1           N2 │
-110000+0 221842+5 858948+1 972320-4-781411+5 637717+2 2500. 6000.1           N2 │
-110000+0 182149+5 699575+1-159687-3-154956+2 615040+2  20.  500.1            N2 │
   1  8   0   0   0   0   0   0   0   0   0   0   0JANAF TAPE 7/71   6/62       O  │
595589+5 135166+5 496176+1 567346-5 298680+5 500932+2 -500. 2500.1            O  │
595589+5 135210+5 450112+1 133922-3 904980+6 500947+2 2500. 6000.1            O  │
595589+5 100863+5 566946+1-117145-2 83475i+2 483605+2  20.  500.1             O  │
   1  7   0   0   0   0   0   0   0   0   0   0   0JANAF TAPE 7/71   3/61       N  │
112964+6 134412+5 492461+1 271364-4 956039+4 480916+2 -500. 2500.1            N  ├─ Note: See Ref. 6 for
112964+6 134277+5 277722+1 523356-3 567729+7 480868+2 2500. 6000.1            N  │        Definitions and
112964+6 135297+5 496142+1 299758-4 246457+1 481461+2  20.  500.1             N  │        Code Input Format
   1  7   1  8                           GILMORE- JANAF                        NO │
215799+5 227508+5 808175+1 354495-3-276336+6 688669+2 -500. 2500.1            NO │
215799+5 227145+5 877301+1 726516-4-192889+6 688541+2 2500. 6000.1            NO │
215799+5 171236+5 750704+1-708686-3 239574+3 657170+2  20.  500.1             NO │
   1 99   0   0   0   0   0   0   0   0   0   0   0CONVAIR ZPH-122 12/61        E- │
          149010+5 4.965                          16.4558  10.  3000. 1        E- │
          149010+5 498851+1-272800-5-135900+6 164558+23000. 10000.1           E- │
   1  7  -1 99   0   0   0   0   0   0   0   0   0CONVAIR ZPH-122 12/61        N+ │
446641+6 151310+5 4.998                          49.6847  10.  3000. 1        N+ │
446641+6 151310+5 501751+1 617100-4-184100+7 496847+23000. 10000.1           N+ │
   1  7   1  8  -1 99   0   0   0   0   0   0   0CONVAIR ZPH-122 12/61        NO+ │
232919+6 241970+5 8.834                          65.4379  10.  3000. 1        NO+ │
232919+6 241970+5 910216+1 277400-4-316600+7 654379+23000. 10000.1           NO+ │
   1  8  -1 99   0   0   0   0   0   0   0   0. 0 CONVAIR ZPH-122 12/61        O+ │
371999+6 149290+5 4.939                          48.4849  10.  3000. 1        O+ │
371999+6 149290+5 336271+1 306710-3 590200+7 484849+23000. 10000.1           O+ ⌐
```

Table A-2. Comparison of Values of Enthalpy at High Temperatures

| Pressure, atm	T, ^oK	Values of Enthalpy, kcal/gm			
		Feigenbutz & Solum (Ref. 34)	Predvoditelev (Ref. 35)	Hansen (Ref. 36)	BLIMP (Ref. 6)
1×10^{-3}	6,000	9.004	8.921	9.04	8.927
	8,000	11.794	11.740	11.88	11.762
	10,000	26.144	26.340	22.61	26.348
1×10^{-2}	6,000	7.903	7.812	7.94	7.810
	8,000	10.538	10.480	10.61	10.497
	10,000	16.762	16.830	17.00	16.890
1×10^{-1}	6,000	5.332	5.250	5.32	5.248
	8,000	10.045	9.984	10.11	9.992
	10,000	12.807	12.790	12.93	12.850
1	6,000	3.640	3.572	3.58	3.573
	8,000	9.143	9.024	9.18	9.025
	10,000	11.461	11.410	11.55	11.473
10	6,000	2.979	2.914	2.93	2.917
	8,000	6.620	6.448	6.58	6.445
	10,000	10.603	10.540	10.71	10.599
100	6,000	2.645	2.570	2.62	2.573
	8,000	4.530	4.401	4.48	4.403
	10,000	8.365	8.296	8.52	8.330

Table A-3. Comparison of Values of Equilibrium Specific Heat
at Constant Pressure at High Temperatures

ρ/ρ_0	T, °K	Values of C_p, cal/gm-°K			
		Feigenbutz & Solum (Ref. 34)	Predvoditelev (Ref. 35)	Brahinsky and Neel (Ref. 31)	BLIMP (Ref. 6)
10^{-4}	6,000	2.1383	2.150	2.2281	2.235
10^{-4}	7,200	0.9145	0.9141	0.9141	0.912
10^{-4}	9,700	5.3633	5.369	5.3100	5.273
10^{-3}	7,300	1.0980	1.099	1.1321	1.135
10^{-3}	8,300	1.0306	1.031	1.0301	1.036
10^{-3}	9,600	2.0892	2.092	2.0770	2.0802
10^{-2}	6,400	3.4651	3.330	3.4023	3.4025
10^{-2}	8,600	1.0432	1.049	1.0683	1.0837
10^{-2}	9,200	0.9927	0.9964	1.0039	1.0233
10^{-2}	9,900	1.1827	1.184	1.1894	1.2117
10^{-1}	7,100	2.6029	2.586	2.5465	2.5417
10^{-1}	8,000	2.8005	2.801	2.8027	2.8087
1	6,000	0.7075	0.7069	0.7041	0.7018
1	6,700	1.0197	1.015	1.0007	0.9982
1	8,100	1.9995	1.981	1.9502	1.9508
1	9,200	2.3263	2.316	2.3009	2.3338
10	7,600	0.8512	0.8475	0.8369	0.8342
10	9,400	1.5353	1.517	1.4914	1.5020
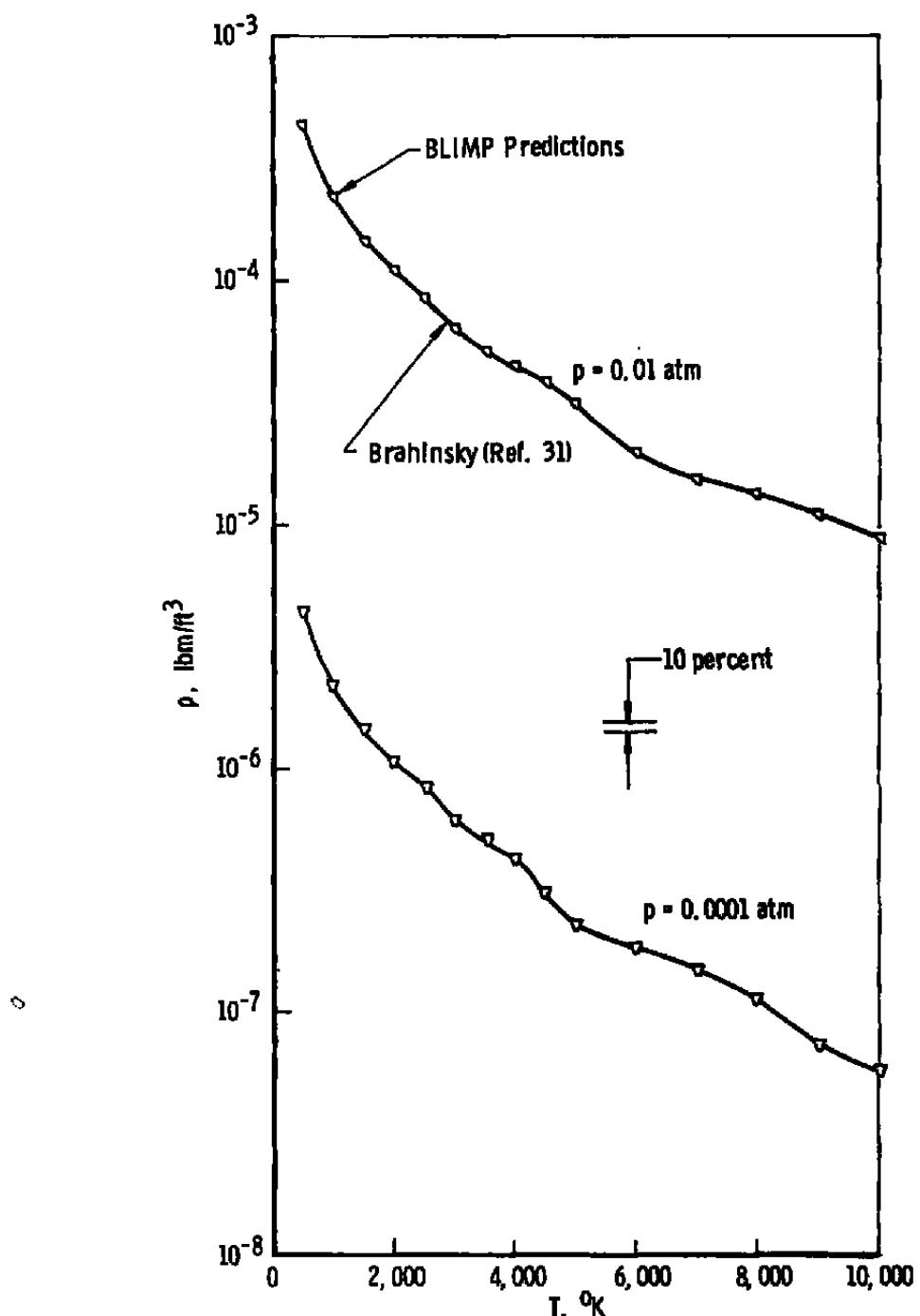
a. At low pressure

Figure A-1. BLIMP calculation of density compared with Brahinsky data.
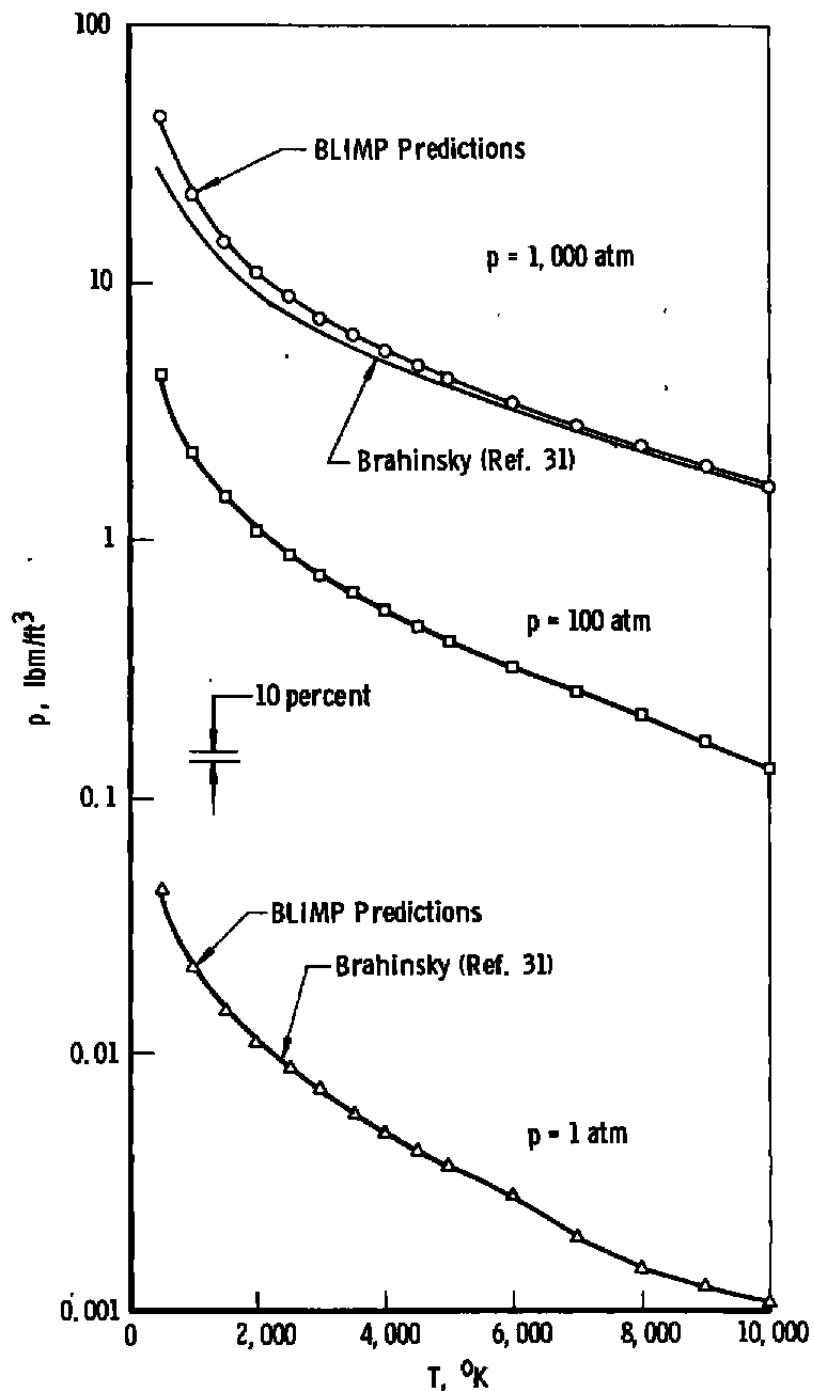
b. At high pressure

Figure A-1. Concluded.
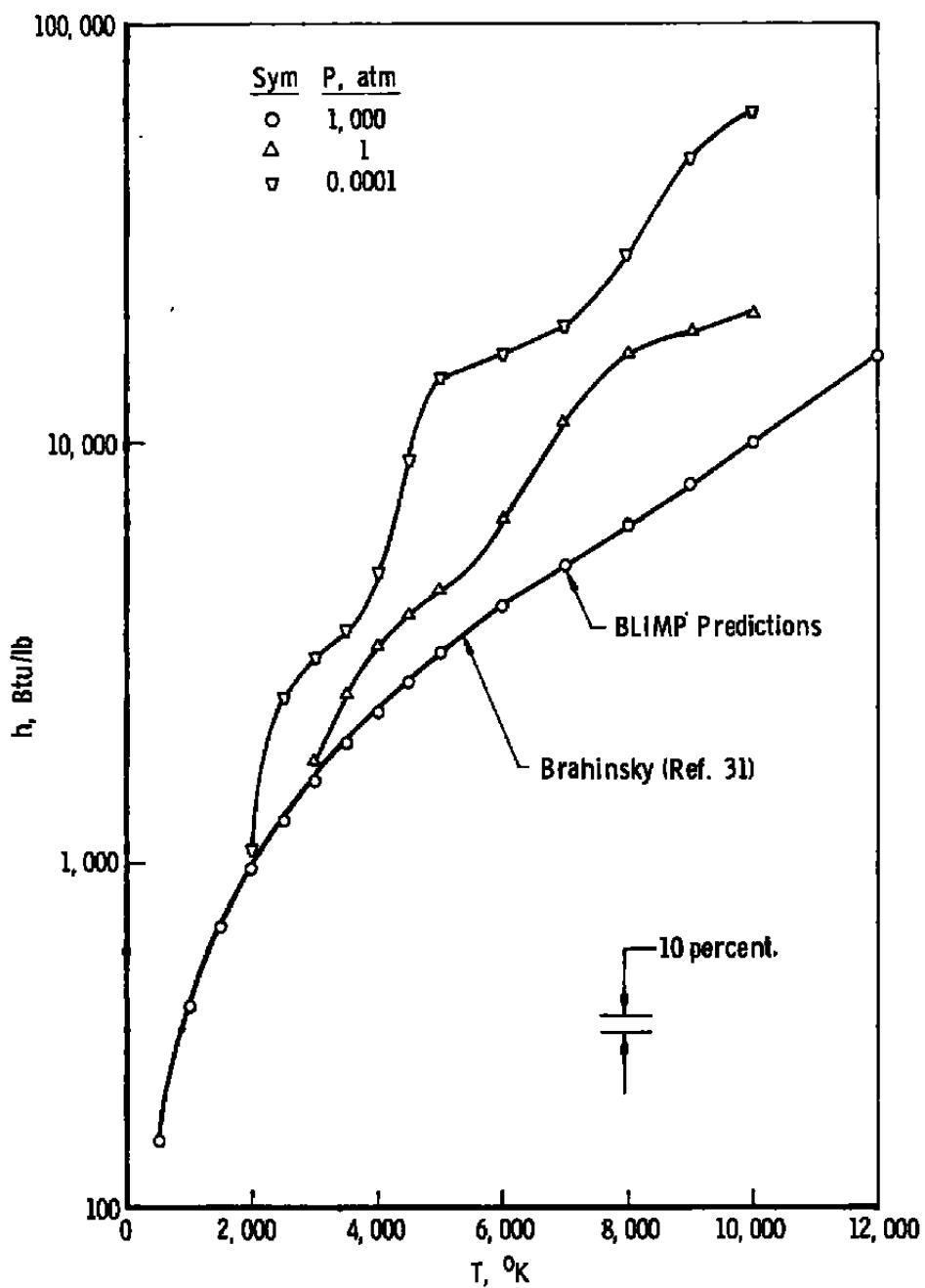
Figure A-2. BLIMP calculation of enthalpy compared with Brahinsky data.
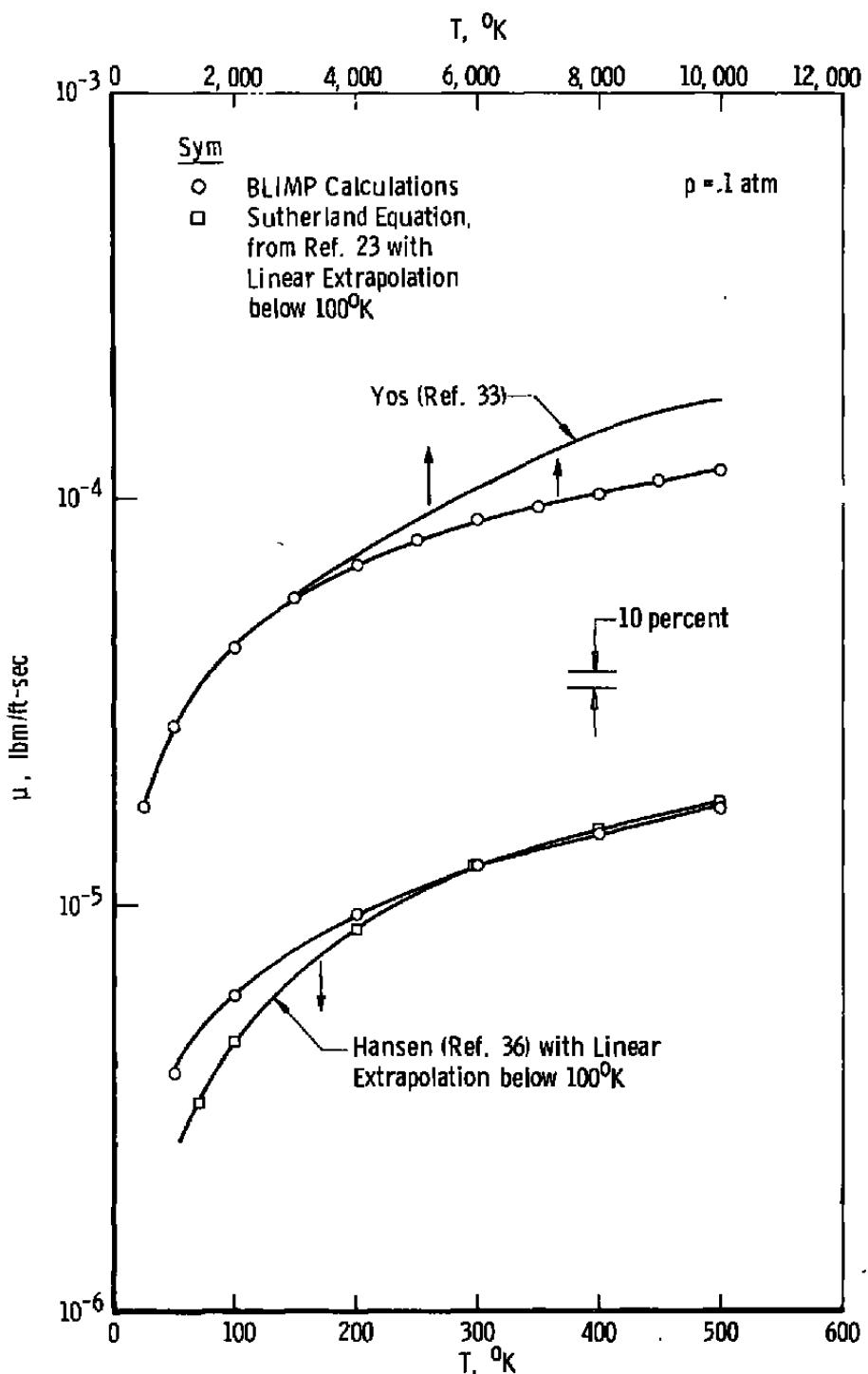
Figure A-3. Comparison of BLIMP calculation of viscosity with theory.
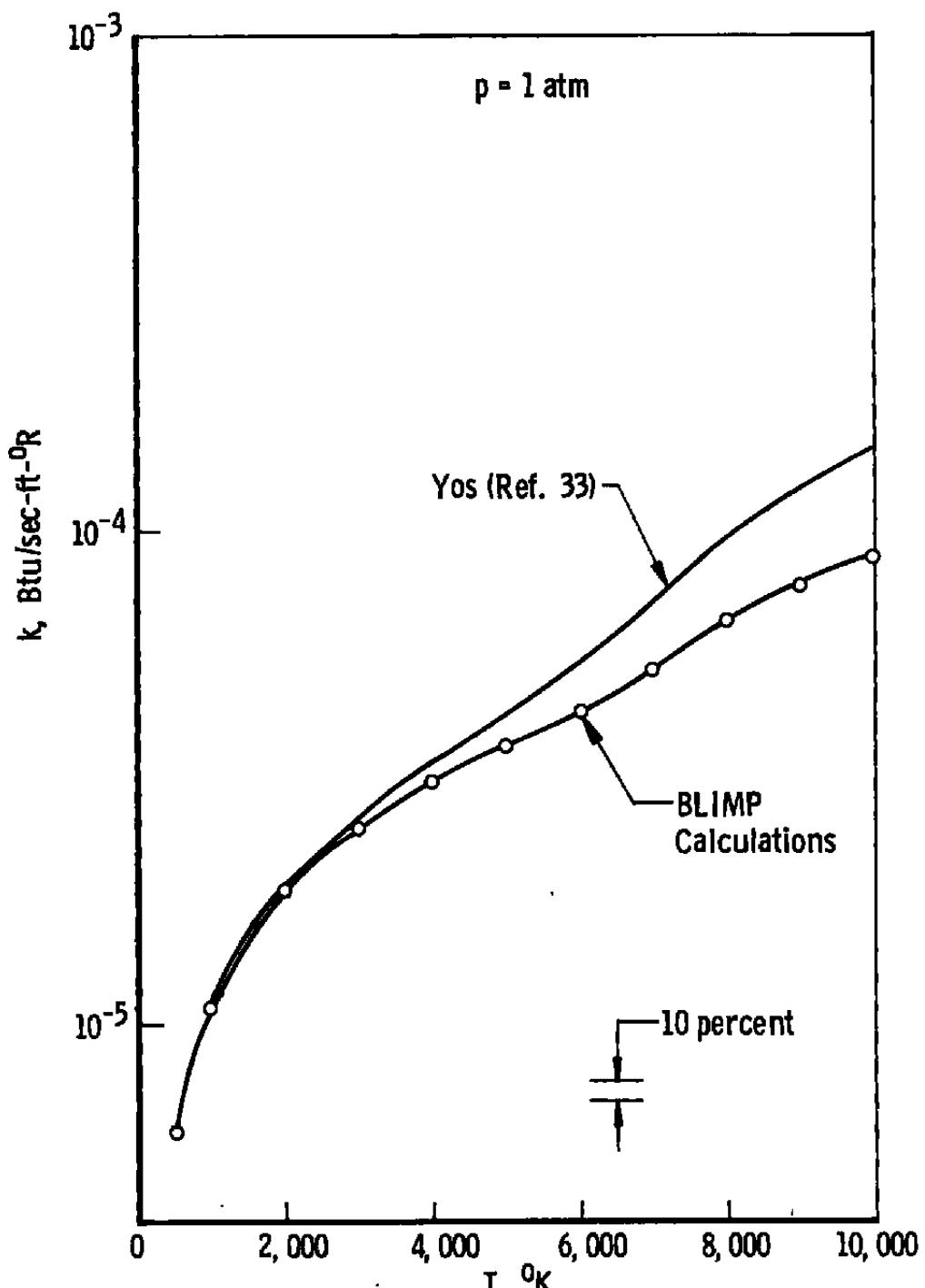
a. High-temperature range

Figure A-4. Comparison of BLIMP calculation of thermal conductivity with theory.

p = 1 atm

Sym

○   BLIMP Calculations

□   Sutherland Equation from Ref. 23 with Pr = 0. 71, C_p = 0. 23989 Btu/lb

10 percent

Hansen, (Ref. 36) with Straight-Line Extrapolation below 100°K
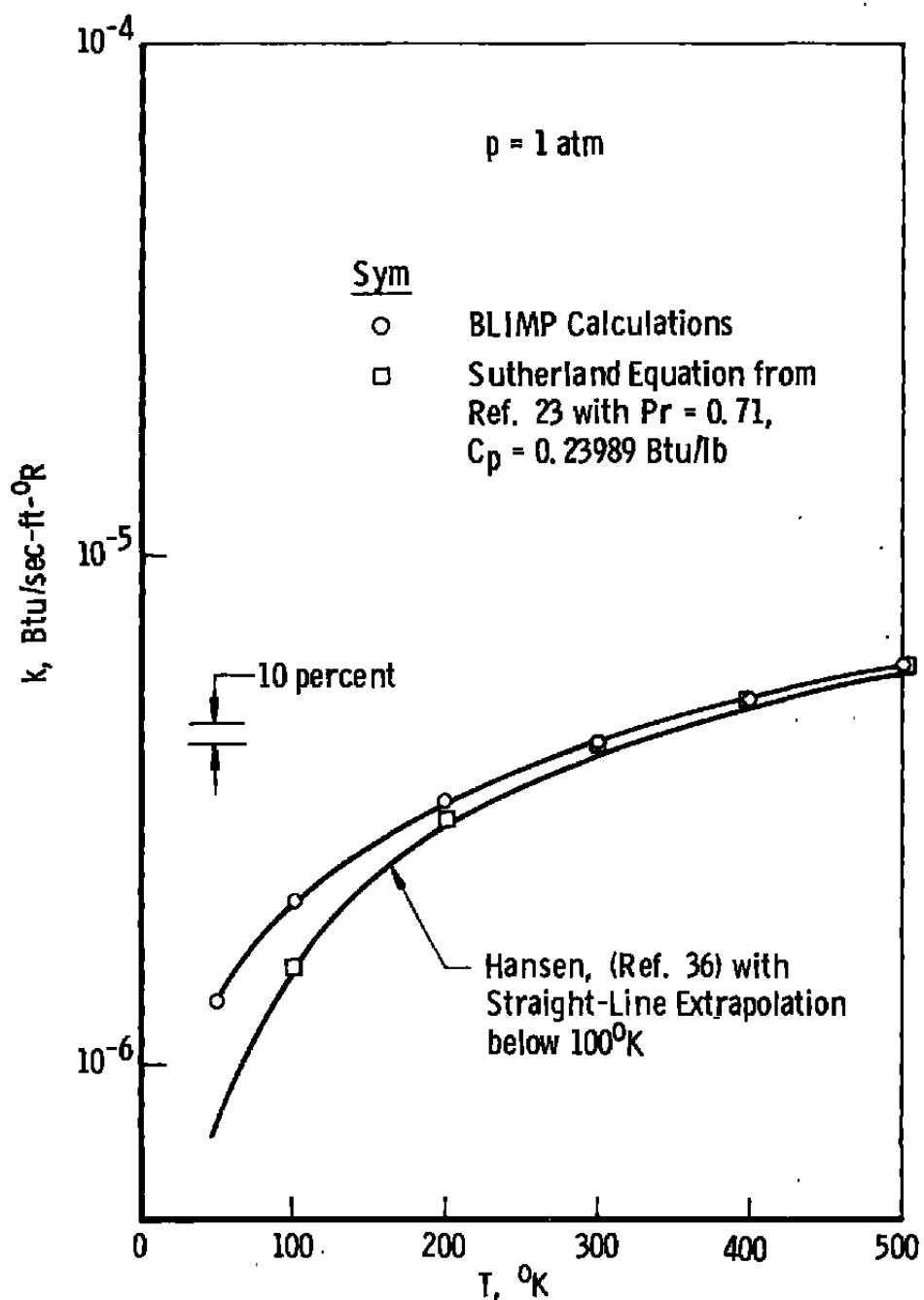
b. Low-temperature range
Figure A-4. Concluded.

NOMENCLATURE

A   Surface area

A_b Base area

A^+ Constant in Eq. (8), 26.0

C_{D_F} Skin friction drag coefficient, $\int \tau_w \cos \theta \, dA/q_\infty A_b$

C_{D_p} Pressure drag coefficient, $\int (p - p_\infty) \sin \theta \, dA/q_\infty A_b$

C_p Specific heat at constant pressure

c   Constant in Eq. (14) or (16), 0.0168 for BLIMP/CEBECI, 0.0180 for BLIMP/KENDALL

h   Spreading factor for angle-of-attack effects, Eq. (18)

h   Static enthalpy

k   Constant in the mixing length equation, Eq. (6), (7), or (8), 0.435 for Patankar-Spalding

k   Constant in the BLIMP/KENDALL mixing length equation, Eq. (10), (11), or (12), 0.44

k   Thermal conductivity

k   Cross-flow parameter, see Eq. (19)

ℓ Mixing length, Eqs. (4) through (8), (10) through (14), (16)

M_∞ Free-stream Mach number

Pr   Prandtl number, $C_p \, \mu/k$

Pr_t Turbulent Prandtl number, $C_p \, \epsilon_m/\epsilon_h$

p   Static pressure

p_o' Total pressure behind a normal shock

q_∞ Free-stream dynamic pressure

$\dot{q}$ Heat-transfer rate

Re_∞ Free-stream Reynolds number

R_N Nose radius

r   Distance measured perpendicular to the body centerline and from the body centerline

r_o Defined by Eq. (20)

S   Distance along the body surface measured from the apex (sharp cone) or stagnation point (blunt body)

T   Temperature

T_e Temperature at the edge of the boundary layer

T_w Wall temperature

u   Streamwise velocity

u_e Velocity at the edge of the boundary layer

u_{e_N} Velocity at the edge of the boundary layer assuming normal shock entropy at the outer edge

u' Fluctuating streamwise velocity

V_t Turbulent velocity ($= u_e$ in Eq. (16))

v' Fluctuating normal velocity

w   Circumferential velocity component

y   Distance perpendicular to the body surface

y_t Total boundary-layer thickness defined as the point where the velocity in the boundary layer is equal to 0.99 of u_e, or in some of the programs the point where the total enthalpy is 0.995 of the free-stream total enthalpy

y^+ Dimensionless normal coordinate defined by Eq. (9)

y_a^+ Constant in Eq. (12) (= 11.823)

Z   Distance along the axis measured from the sharp cone apex or from a blunt body stagnation point

Z_o Constant in Eqs. (18) and (20)

α Angle of attack

γ Ratio of specific heats

Δ_S Increment in entropy from normal shock value

δ Boundary-layer thickness

δ^* Boundary-layer displacement thickness

δ_i^* Incompressible boundary-layer displacement thickness, Eq. (15)

ϵ_h Eddy thermal conductivity

ϵ_m Eddy viscosity

θ Boundary-layer momentum thickness

θ Body surface angle, referenced to a line parallel to the body centerline

θ_c Cone half-angle

λ Outer law mixing constant, 0.090, Eq. (13)

μ Molecular viscosity

ϱ Density

ϱ_0 Density at standard conditions of $p = 1$ atm, $T = 273.15°K$

τ Shear stress

τ_w Wall shear stress

ν Kinematic viscosity

ϕ Circumferential angle; $\phi = 0$ is windward plane of symmetry

SUBSCRIPTS

e   Edge of the boundary layer

w   Wall condition

∞ Free-stream condition

SUPERSCRIPT

$'$ Fluctuating quantity, (except p_0')

$-$ Quantity averaged with respect to time